

# Energetics of Divalent Selectivity in a Calcium Channel: The Ryanodine Receptor Case Study

Dirk Gillespie

Department of Molecular Biophysics and Physiology, Rush University Medical Center, Chicago, Illinois

**ABSTRACT** A model of the ryanodine receptor (RyR) calcium channel is used to study the energetics of binding selectivity of  $\text{Ca}^{2+}$  versus monovalent cations. RyR is a calcium-selective channel with a DDDD locus in the selectivity filter, similar to the EEEE locus of the L-type calcium channel. While the affinity of RyR for  $\text{Ca}^{2+}$  is in the millimolar range (as opposed to the micromolar range of the L-type channel), the ease of single-channel measurements compared to L-type and its similar selectivity filter make RyR an excellent candidate for studying calcium selectivity. A Poisson-Nernst-Planck/density functional theory model of RyR is used to calculate the energetics of selectivity.  $\text{Ca}^{2+}$  versus monovalent selectivity is driven by the charge/space competition mechanism in which selectivity arises from a balance of electrostatics and the excluded volume of ions in the crowded selectivity filter. While electrostatic terms dominate the selectivity, the much smaller excluded-volume term also plays a substantial role. In the D4899N and D4938N mutations of RyR that are analyzed, substantial changes in specific components of the chemical potential profiles are found far from the mutation site. These changes result in the significant reduction of  $\text{Ca}^{2+}$  selectivity found in both theory and experiments.

## INTRODUCTION

Calcium-selective ion channels play an important role in many physiological functions including in the excitation-contraction coupling pathway that links surface membrane excitation and calcium-dependent muscle contraction. For example, cardiac muscle excitation-contraction coupling involves two kinds of calcium channels: depolarization of the transverse tubule activates the voltage-dependent L-type calcium channel (also known as the dihydropyridine receptor) that generates a  $\text{Ca}^{2+}$  influx that activates nearby ryanodine receptor (RyR) calcium channels. RyR, in turn, conducts  $\text{Ca}^{2+}$  out of the sarcoplasmic reticulum, a  $\text{Ca}^{2+}$ -storage organelle. It is this large  $\text{Ca}^{2+}$  release that regulates muscle contraction.

The L-type and RyR calcium channels have very different physiological functions. The L-type channel mediates a relatively small  $\text{Ca}^{2+}$  flux to locally activate RyR while RyR mediates a large  $\text{Ca}^{2+}$  flux to globally elevate cytosolic  $[\text{Ca}^{2+}]$ . To accomplish these functions, the L-type and RyR calcium channels have very different permeation and selectivity properties: the L-type channel has a small conductance (1) and micromolar  $\text{Ca}^{2+}$  affinity (2,3) while RyR has a large conductance and only millimolar  $\text{Ca}^{2+}$  affinity (4). On the other hand, both the L-type and RyR calcium channels have negatively-charged, carboxyl-rich selectivity filters, namely the EEEE locus of L-type (5,6) and the DDDD locus of RyR (with additional loci of glutamates and aspartates in the vestibules playing supporting roles) (7). Therefore, it is plausible that both channels share a mechanism for selectivity that is determined by the EEEE/DDDD locus. In this article, a

model of RyR is used to understand how an EEEE/DDDD locus leads to a  $\text{Ca}^{2+}$ -selective channel. RyR is used because a model of permeation through it already exists (and is expanded on here) and because it is relatively easy to perform single-channel measurements, providing a very large data set to work with.

Selectivity in calcium channels has been modeled most recently with general studies by Boda and co-workers (including the author) (8–12), specific studies of the L-type channel by Nonner and co-workers (13,14) and Corry et al. (15,16), and RyR by Chen et al. (17–19) and the author (20). From these studies, two schools of thought have emerged with regard to why calcium channels prefer to bind/conduct  $\text{Ca}^{2+}$  over high levels of background monovalent cations. Corry et al. (15,16) argue that the L-type channel must be a single-filing channel and that  $\text{Ca}^{2+}$  is preferred because calcium ions see a much larger electrostatic energy-well from the four glutamates than monovalent ions (16). In their model, the glutamates are not in physical contact with the permeating ions. On the other hand, Nonner, Boda, the author, and co-workers argue that calcium channels have a small (but not single-filing) and crowded selectivity filter with the glutamates in the pore lumen directly interacting with the permeating ions. Their channel prefers  $\text{Ca}^{2+}$  over monovalent cations because of the balance of electrostatic and excluded-volume forces (i.e., two ions cannot overlap) (8–12,14,20–22). For example, two  $\text{Ca}^{2+}$  can balance the four negative glutamates in half the volume of four  $\text{Na}^+$ , a mechanism called charge/space competition (CSC).

Both schools argue that they qualitatively reproduce the important characteristics of the L-type channel (e.g., the anomalous mole fraction effect, AMFE, where micromolar concentrations of  $\text{Ca}^{2+}$  block  $\text{Na}^+$  current), but both have

*Submitted July 6, 2007, and accepted for publication September 18, 2007.*

Address reprint requests to Dirk Gillespie, Tel.: 312-942-3089; E-mail: dirk\_gillespie@rush.edu.

Editor: Peter C. Jordan.

© 2008 by the Biophysical Society  
0006-3495/08/02/1169/16 \$2.00

doi: 10.1529/biophysj.107.116798

problems in fully testing their hypotheses. For example, it was not practical for Corry et al. (15) to simulate the low voltages and low  $\text{Ca}^{2+}$  concentrations where almost all experiments have been done. Instead, they extrapolated four orders of magnitude between their simulation data at 18 mM  $\text{Ca}^{2+}$  to 1  $\mu\text{M}$   $\text{Ca}^{2+}$  where the AMFE is experimentally observed. (A later grand canonical scheme that might allow simulations of lower concentrations (23) has not been applied to calcium channels (16).) Moreover, they only simulated  $\text{Ca}^{2+}$  versus  $\text{Na}^+$  selectivity and did not simulate other monovalent cations to see if their theory is consistent with experiments. They also did not simulate monovalent versus monovalent selectivity (e.g.,  $\text{Na}^+$  versus  $\text{K}^+$ ). This makes it difficult to determine by what mechanism their model channel distinguishes between monovalents, which they are known to do (1); a priori, electrostatics alone would not seem to be enough. Moreover, the physical forces used by a channel to distinguish one monovalent from another must also be present in divalent versus monovalent selectivity. Monovalent versus monovalent selectivity is likely a point where the two models give qualitatively different results.

On the other hand, much of the work on the CSC mechanism has been done with equilibrium simulations that do not compute current, but only channel occupancy (8–12,14). When current was computed, it required data-fitting of excess chemical potentials (see below) (13,18,19)—rather than using a theory to compute them as is done here—which gave reasonable values for these potentials and reproduced the AMFE of the L-type channel (14). Much of the effort by the CSC school has been directed at studying a wide range of selectivity including  $\text{Ca}^{2+}$  versus different monovalents (9,14,21) and monovalent versus monovalent selectivity (9,12) to show that a crowded filter prefers small, high-valence cations. In recent work, they have also shown that reducing both the pore radius and the protein polarization can account for the very different  $\text{Ca}^{2+}$  affinities observed in L-type and RyR channels (11,12). These studies have shown mechanisms that work in principle. Recent mutations of OmpF porin have started to experimentally verify these predictions (24–26).

To move these theories beyond “in principle”, a model of a real calcium channel that reproduces—and predicts—the experimental data over a wide range of ionic conditions and mutations is vital. Many models can account for selectivity under a small set of conditions, but to distinguish between them and to have confidence in any model, a large experimental data set is necessary. In this article, a model that quantitatively reproduces and predicts RyR experimental data in over 100 different ionic solutions is used to study the energetics of selectivity in RyR. The experimental verification of one of these predictions is also shown here. Specifically, the model predicted AMFEs between  $\text{Ca}^{2+}$  and two monovalent cations ( $\text{Na}^+$  and  $\text{Cs}^+$ ):  $\text{Cs}^+$  current is reduced by  $\sim 60\%$  when  $\text{Ca}^{2+}$  is added and  $\text{Na}^+$  current is reduced by  $\sim 50\%$  when  $\text{Ca}^{2+}$  is added. These AMFEs are

large, but not as dramatic as the  $>90\%$  reduction found in the L-type calcium channel (2).

The Poisson-Nernst-Planck/density functional theory (PNP/DFT) model used here computes quickly (minutes for a whole current/voltage curve), computes the excess chemical potentials from thermodynamic formulas, and uses exactly nine experimental data points to determine the ion diffusion coefficients of seven ion species. Another advantage of the PNP/DFT model is that it naturally computes the components of the chemical potential of the ions. That decomposition is used here to dissect  $\text{Ca}^{2+}$  versus monovalent selectivity in both native and mutant RyR. It is found that different terms are important under different circumstances. Also, in mutations differences between mutant and native can extend 7.5 Å beyond the mutation site. The results indicate the  $\text{Ca}^{2+}$  versus monovalent cation selectivity in RyR is driven by the CSC mechanism.

## THEORY AND METHODS

### The Poisson-Nernst-Planck/density functional theory model

The flux through the RyR pore is described by a constitutive relationship that is a generalization of the Poisson-Nernst-Planck (PNP) equations (27–30),

$$-\mathbf{J}_i(\mathbf{x}) = \frac{1}{kT} D_i(\mathbf{x}) \rho_i(\mathbf{x}) \nabla \mu_i(\mathbf{x}), \quad (1)$$

where  $\mathbf{J}_i$ ,  $D_i$ ,  $\rho_i$ , and  $\mu_i$  are the local flux density, diffusion coefficient, density, and chemical potential, respectively, of ion species  $i$ . The value  $k$  is the Boltzmann constant and  $T$  is the temperature. The chemical potential is decomposed into different terms (14,22,31–35),

$$\begin{aligned} \mu_i(\mathbf{x}) = & \overbrace{kT \ln \left( \frac{\rho_i(\mathbf{x})}{\Lambda_i^3} \right)}^{\text{ideal gas}} + \overbrace{z_i e \phi(\mathbf{x})}^{\text{mean electrostatic}} \\ & + \overbrace{\mu_i^{\text{SC}}(\mathbf{x})}^{\text{screening}} + \overbrace{\mu_i^{\text{HS}}(\mathbf{x})}^{\text{excluded volume}}, \end{aligned} \quad (2)$$

where  $e$  is the elementary charge and where the length scale is the de Broglie wavelength  $\Lambda_i$  (36) and  $z_i$  is the valence of ion species  $i$ .

In this decomposition of the chemical potential, there are two electrostatic terms and an excluded-volume term in addition to the usual ideal gas term. The mean electrostatic potential  $\phi$  is given by the average (i.e., long-time, many-particle ensemble average) ion densities via the Poisson equation,

$$-\epsilon_0 \nabla \cdot (\epsilon(\mathbf{x}) \nabla \phi(\mathbf{x})) = e \sum_i z_i \rho_i(\mathbf{x}), \quad (3)$$

where  $\epsilon_0$  is the permittivity of free space and  $\epsilon$  is the local dielectric coefficient. The sum on the right-hand side includes both the densities of the permeating ions and the protein charge densities. If the chemical potential is defined with only the ideal gas and mean electrostatic terms, then Eqs. 1 and 3 reduce to the normal PNP equations of charged, point ions.

The mean electrostatic potential is only part of the electrostatics in electrolytes. To compute ion density profiles, the electrostatic potential that should be used is, in principle, given by the Poisson equation with conditional concentrations (not average) on the right-hand side of Eq. 3. These conditional concentrations are the concentration of species  $i$  at  $\mathbf{x}$  given an ion of species  $j$  fixed at location  $\mathbf{y}$  (the “fixed ion”) and can be expressed

via pair correlation functions (30,35). This conditional concentration profile is the result of how well all the ions within a screening (Debye) length of the fixed ion arrange around it. Intuitively,  $\mu_i^{\text{SC}}(x)$  describes an ion's ability to screen the charge of another ion. In general, a smaller or higher-valence ion screens a charge more efficiently than a larger or lower-valence ion. (Ions with strong polarizability or stronger van der Waals attractions are expected to be even better "screeners", but these properties would have second-order effects compared to size and valence.) This ionic screening is due to interactions on the atomic timescale while the mean electrostatic potential is averaged over the permeation timescale of microseconds. For example, in the bath the mean electrostatic potential is zero because—averaged over microseconds—there is local charge neutrality at every location; the mean potential does not reflect that  $\text{Ca}^{2+}$  and  $\text{Cl}^-$  form different local structures than  $\text{K}^+$  and  $\text{Cl}^-$  in the "homogeneous" bulk. A well-known approximation of this term (not used here) is the Debye/Hückel theory (35,37). In the DFT, this conditional concentration approach is approximated by splitting the electrostatics into the mean electrostatic and screening terms as described (22,33,34,38,39).

The last term in Eq. 2 describes the energy required to insert an uncharged ion at any location into a fluid of uncharged, hard spheres with the same density profile  $\rho_i(x)$  as the ionic fluid. In this article, ions are modeled as charged, hard spheres and water as an uncharged, hard sphere, and therefore excluded volume is purely due to hard-sphere (HS) repulsion. The screening term also includes ion size, but is much less sensitive to changes in ion size than the excluded-volume term (see below).

Both the screening and excluded-volume terms are computed using DFT of classical fluids (not electron orbitals). DFT is currently one of the state-of-the-art theories in physics of confined fluids (e.g., see the reviews (36) and (32)). The specific DFT of charged, hard spheres used here has been tested against multiple Monte Carlo simulations to assess its accuracy (22,34,39,40).

The work shown in this article is computed with a one-dimensional approximation of Eqs. 1–3 that was described previously (13,41) where the dielectric coefficient  $\epsilon$  was constant at 78.4 throughout the system,

$$-J_i = \frac{1}{kT} D_i(x) A(x) \rho_i(x) \frac{d\mu_i}{dx}, \quad (4)$$

$$-\frac{\epsilon \epsilon_0}{A(x)} \frac{d}{dx} \left( A(x) \frac{d\phi}{dx} \right) = e \sum_i z_i \rho_i(x), \quad (5)$$

where the flux  $J_i$  is now a constant and  $A(x)$  is the area of the equi-chemical potential surfaces that is estimated as previously described (13,41). The equations for the excess chemical potentials may be found in the literature (22,34). They are not reproduced here because they are long and the formulas by themselves do not provide any obvious physical insight.

## Model of the pore

The geometry of the model RyR pore is shown in Fig. 1. Only five amino acids of the RyR protein are explicitly modeled: Asp-4899, Glu-4900, Asp-4938, Asp-4945, and Glu-4902. In mutation experiments, these were found to be the only conserved, charged amino acids near the selectivity filter that affected permeation and/or selectivity (7,42,43).

The pore contains a 15 Å-long selectivity filter (10 Å <  $x$  < 25 Å) flanked by two atria. Starting near the selectivity filter, the atrium on the cytosolic side (0 Å <  $x$  < 10 Å) widens into a cavity 14 Å in diameter where Asp-4938 is located. The rest of the RyR protein on the cytosolic side is not modeled and the cavity is connected to the bath by a widening conical pore (−10 Å <  $x$  < 0 Å) that contains Asp-4945. On the other side of the pore, a similar conical pore (25 Å <  $x$  < 32 Å) contains Glu-4900 and connects the selectivity filter to the luminal bath. Asp-4899, which showed the largest change in conductance and selectivity in mutation experiments, is located in the selectivity filter.

A permeant cation is given a different diffusion coefficient in each region. To illustrate, the diffusion coefficients for  $\text{K}^+$  are presented here (for the

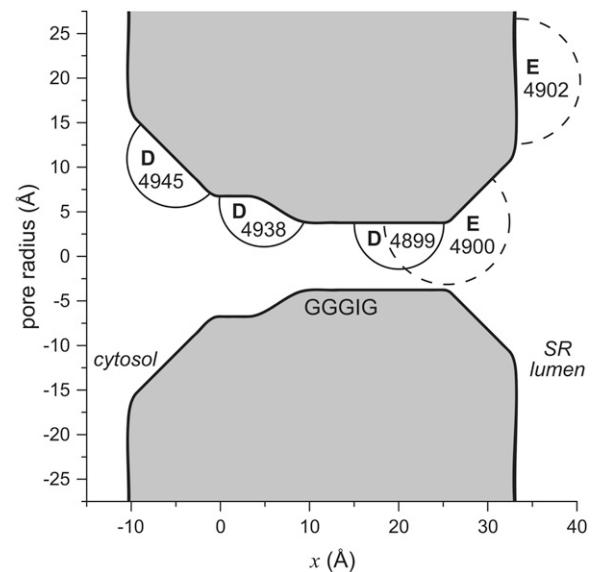


FIGURE 1 The geometry of the model RyR pore. In the experiments and calculations, the lumen of the sarcoplasmic reticulum (SR) is electrically grounded. The circle around each labeled amino acid is meant to illustrate the range of the motion of the terminal carboxyl group. Aspartates (solid circles) are given a radius of 5 Å and glutamates (dashed circles) 7 Å. Only the amino acids of one of the four identical RyR subunits is shown. Asp-4945, Asp-4938, Asp-4899, Glu-4900, and Glu-4902 are the only amino acids explicitly modeled in the theory. The GGGIG sequence (4894–4898 in the numbering) at the cytosolic end of the selectivity filter is only a reference point for readers familiar with the RyR sequence.

other ions, see Appendix). In the cytosolic cavity, the diffusion coefficient of  $\text{K}^+$  is 61% of the bulk diffusion coefficient. This is consistent with this being a wide part of the channel. The selectivity filter is the narrowest part of the model pore and is therefore expected to be the place where ion flux is limited; the diffusion coefficient is made smallest there ( $6.91 \times 10^{-11} \text{ m}^2/\text{s}$ ). In the widening luminal atrium, it is 5.83 times larger than in the selectivity filter. For the seven permeant cations considered in this article ( $\text{Li}^+$ ,  $\text{Na}^+$ ,  $\text{K}^+$ ,  $\text{Rb}^+$ ,  $\text{Cs}^+$ ,  $\text{Ca}^{2+}$ , and  $\text{Mg}^{2+}$ ) exactly nine data points were used to determine their diffusion coefficients in the pore, as described in the Appendix. The selectivity filter diffusion coefficients were found to be 1–4% of bulk values for the monovalent cations and 0.5% of bulk for the divalents.

Comparisons of the model with experimental data are shown in the Supplementary Material. The Supplementary Material also discusses the model's self-consistency and possible errors.

## Analysis of binding selectivity

The energetics of ion binding within the pore is most easily analyzed in equilibrium when no currents from any ion species are flowing (i.e.,  $J_i = 0$  for all ion species) and the chemical potential is constant throughout the system (in the baths and the pore):

$$\mu_i^{\text{bath}} = \mu_i^{\text{pore}}(x). \quad (6)$$

In this article, the baths are identical in concentration and composition, and all the analysis of selectivity is done in equilibrium based on the decomposition of the chemical potential described above (Eq. 3).

## AMFE experiments

The experimental results shown in Fig. 2 were measured by the lab of Michael Fill (Rush University Medical Center) using standard, previously

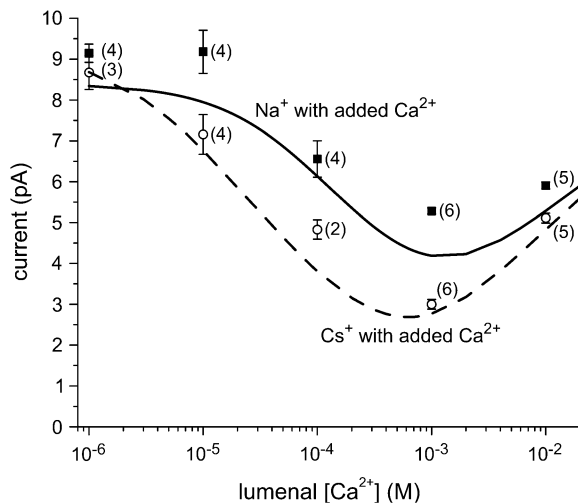


FIGURE 2 Experimental verification of the AMFE predicted by the theory. The lines are the theory and the symbols are the experimental data with standard error bars and the number of experiments in parentheses. The solid line and symbols are the addition of  $Ca^{2+}$  to  $Na^+$  and the dashed line and open symbols are the addition of  $Ca^{2+}$  to  $Cs^+$ . In all cases, the monovalent-chloride concentration was 100 mM in both cytosolic and luminal baths and the indicated amount  $Ca^{2+}$  was added to the luminal bath. The current at  $-20$  mV is shown.

described methods (44). These experiments were performed on the cardiac isoform (RyR2) that still had regulatory proteins (e.g., the negatively-charged calsequestrin) attached to them. In this way, these channels are different from the “purified” RyR channels for which the theory was originally developed (20,42,43). This may contribute to the larger discrepancies between theory and experiment than those shown in Supplementary Material Figs. S1–S9. Nevertheless, the model is in very good agreement with experiment. The experiments were performed after the theoretical calculations to test the predictive power of the model. No parameters were changed in the model to better reproduce the experimental data.

## RESULTS

### AMFE for $Ca^{2+}$ and monovalent cations

Several mole fraction experiments have been performed in RyR, both for mixtures of monovalent cations with other monovalents and mixtures of divalents with other divalents (45,46). In these experiments, the relative concentrations of two ion species was changed while the total concentrations of both species was kept constant and the conductance was measured as a function of mole fraction. None of these experiments showed a minimum (an AMFE) until the RyR model of Gillespie et al. (20) predicted an AMFE for mixtures of  $Na^+$  and  $Cs^+$ . This was experimentally verified after the model calculations were done (Supplementary Material Fig. S7A).

Here another AMFE prediction of the RyR model is presented, this time in mixtures of  $Ca^{2+}$  and  $Cs^+$  as well as  $Ca^{2+}$  and  $Na^+$ . Because millimolar  $Ca^{2+}$  concentration on the cytosolic side of RyR decreases open probability (47), it is not possible to perform mole fraction experiments with

symmetric bath conditions. Instead, the protocol is that of Almers et al. (2), who used symmetric, fixed concentrations of a monovalent cation and only increased luminal  $[Ca^{2+}]$ . This protocol produced the classical AMFE in the L-type calcium channel that showed the block of  $Na^+$  current by micromolar  $Ca^{2+}$  (2,3).

The calculations were completed—with all model parameters fixed—before the experiments were performed. The model predicted not only the presence of a minimum, but also that the minimum for  $Cs^+$  would be deeper than for  $Na^+$ . Specifically, the theory predicted a reduction in current of 47% for  $Na^+$  at 1 mM  $Ca^{2+}$  (compared to 1  $\mu$ M  $Ca^{2+}$ ) and a 59% reduction in current for  $Cs^+$ . The experimental results were 42% and 65%, respectively (Fig. 2). Moreover, the theory predicted that 10  $\mu$ M  $Ca^{2+}$  added to  $Na^+$  would not substantially change the net current (Fig. 2, the two *left-most squares*) while 10  $\mu$ M  $Ca^{2+}$  added to  $Cs^+$  would decrease net current by  $\sim 20\%$  (Fig. 2, the two *left-most circles*). These results and those shown in the Supplementary Material Fig. S9 indicate that the model can accurately reproduce  $Ca^{2+}$  versus monovalent cation selectivity data over a very wide range of conditions (i.e., 0–50 mM  $Ca^{2+}$ ;  $-150$  to  $+150$  mV applied voltage;  $Na^+$ ,  $K^+$ , and  $Cs^+$  as monovalents). Under the same conditions, the model also predicts a significant AMFE for mixtures of  $K^+$  and  $Ca^{2+}$ , but only a small minimum for mixtures of  $Li^+$  and  $Ca^{2+}$ . These experiments have not been performed yet.

More study is planned to understand the molecular origin of the AMFE in RyR. However, the calculations show that the AMFE in RyR does not require the correlated motion of multiple ions through a long, single-filing pore (48); the model pore does not include a single-filing selectivity filter (it is 8 Å in diameter). Moreover, the model does not include the conservation of momentum necessary to model correlated ion motion; the Nernst-Planck equation used to describe ion flux (Eq. 1) only includes conservation of mass (49,50). In general, the physical interpretations of the AMFE are highly model-dependent. Because classical barrier models of ion permeation do not include the physics known to exist in electrolytes, using these models to infer the occupancy—or any property—of a channel is problematic (13,17,51–53).

### Dependence of $Ca^{2+}$ versus $K^+$ selectivity on bath $Ca^{2+}$ concentration

To study binding selectivity (i.e., the amount of an ion species that accumulates at one location in the pore), the equilibrium case of identical baths is considered. Then, the partitioning of ion species  $i$  between the bath and location  $x$  in the pore can be written as

$$\ln\left(\frac{\rho_i(x)}{\rho_i^{\text{bath}}}\right) = -\frac{z_i e}{kT} \phi(x) - \frac{\Delta\mu_i^{\text{SC}}(x)}{kT} - \frac{\Delta\mu_i^{\text{HS}}(x)}{kT}, \quad (7)$$

where  $\mu_i^{\text{SC}}(x)$  indicates the screening chemical potential at  $x$  minus the bath value (and similarly for the HS term). Each of these terms are shown in Figs. 3–6 for a bath containing 150 mM KCl and varying amounts of  $\text{CaCl}_2$  ranging from 1  $\mu\text{M}$  to 50 mM. In Figs. 4–6, a negative term favors partitioning from the bath into the pore while a positive term indicates that for this component the ion is more energetically stable in the bath.

Fig. 3 shows the partitioning coefficient plotted logarithmically (the left-hand side of Eq. 7) for  $\text{K}^+$  and  $\text{Ca}^{2+}$ . For  $\text{K}^+$  (Fig. 3 A), the bath concentration is held constant and so the decrease in partitioning as  $[\text{Ca}^{2+}]$  increases is a direct result of  $\text{K}^+$  being replaced by  $\text{Ca}^{2+}$  everywhere within the pore. For  $\text{Ca}^{2+}$  (Fig. 3 B), on the other hand, partitioning reflects not only an increase in  $\rho_{\text{Ca}}(x)$  within the pore, but also an increase in bath  $[\text{Ca}^{2+}]$ . Even though more and more  $\text{Ca}^{2+}$  enters the pore as  $[\text{Ca}^{2+}]$  increases, the ratio of  $\rho_{\text{Ca}}(x)$  to  $[\text{Ca}^{2+}]$ —the partitioning—decreases as more  $\text{Ca}^{2+}$  is added to the bath; the increase of  $\text{Ca}^{2+}$  concentration in the pore is proportionately smaller than the increase of  $\text{Ca}^{2+}$  concentration in the baths.

Fig. 4 shows the mean electrostatic component  $z_i e \phi(x)$  in Eq. 7. Because  $\text{Ca}^{2+}$  has twice the charge of  $\text{K}^+$ , this component is twice as large for  $\text{Ca}^{2+}$  (Fig. 4 B) as for  $\text{K}^+$  (Fig. 4 A). For both ion species, this term makes up much more than half of the partitioning. Also, it is important to note that  $\phi(x)$  changes from a deep well in the selectivity filter when  $[\text{Ca}^{2+}]$  is low to being very close to zero throughout the channel when  $[\text{Ca}^{2+}]$  is high; the mean electrostatic potential changes significantly as  $[\text{Ca}^{2+}]$  changes. This indicates that the entire pore is becoming more and more charge-neutral (on average over a long time and many particles passing through the channel) as  $[\text{Ca}^{2+}]$  is increased. It must be the entire pore that is becoming electroneutral, because any significant net charge in any region of the pore would create an electrostatic potential well or barrier in the electrostatic potential profile computed from the Poisson equation (Eq. 3).

Fig. 5 shows the screening component of the partitioning  $\mu_i^{\text{SC}}(x)$  in Eq. 7 that describes the electrostatics beyond the mean electrostatic component with a perturbation expansion of the mean spherical approximation of electrolytes (21,34).  $\text{Ca}^{2+}$  (Fig. 5, *dashed lines*) has a much more negative screening term compared to the slightly negative screening term for  $\text{K}^+$  (Fig. 5, *solid lines*);  $\text{Ca}^{2+}$  is more efficient than  $\text{K}^+$  at screening the protein charges in the pore. This component of the partitioning is always negative (favoring partitioning into the pore) and changes little as  $[\text{Ca}^{2+}]$  increases.

Fig. 6 shows the hard-sphere (HS) component  $\Delta\mu_i^{\text{HS}}(x)$  in Eq. 7 that describes the contribution of the ions' excluded volume. This excluded-volume term is positive, indicating that it is more difficult to insert an ion-sized particle into the selectivity filter than into the bath. The size of the ions hinders ion partitioning into the pore from the bath. This term is, however, small in the pore ( $<1$  kT). Like the screening term,  $\Delta\mu_i^{\text{HS}}(x)$  changes little as  $[\text{Ca}^{2+}]$  increases.

While these profiles are useful for understanding the partitioning of one ion species into the pore, by themselves they do not show why one ion species is favored over another because they do not directly compare two ion species. For this, the difference in the partitioning between the two ion species ( $\text{K}^+$  and  $\text{Ca}^{2+}$  in this example) is necessary. Specifically, the relative concentrations in the pore are considered:

$$\ln \left( \frac{\rho_{\text{Ca}}(x)}{\rho_{\text{K}}(x)} \right) = \underbrace{\ln \left( \frac{[\text{Ca}^{2+}]}{[\text{K}^+]} \right)}_{\text{number advantage}} + \underbrace{(z_{\text{K}} - z_{\text{Ca}}) \frac{e\phi(x)}{kT}}_{\text{mean electrostatic advantage}} + \underbrace{\frac{1}{kT} (\Delta\mu_{\text{K}}^{\text{SC}}(x) - \Delta\mu_{\text{Ca}}^{\text{SC}}(x))}_{\text{screening advantage}} + \underbrace{\frac{1}{kT} (\Delta\mu_{\text{K}}^{\text{HS}}(x) - \Delta\mu_{\text{Ca}}^{\text{HS}}(x))}_{\text{excluded-volume advantage}}. \quad (8)$$

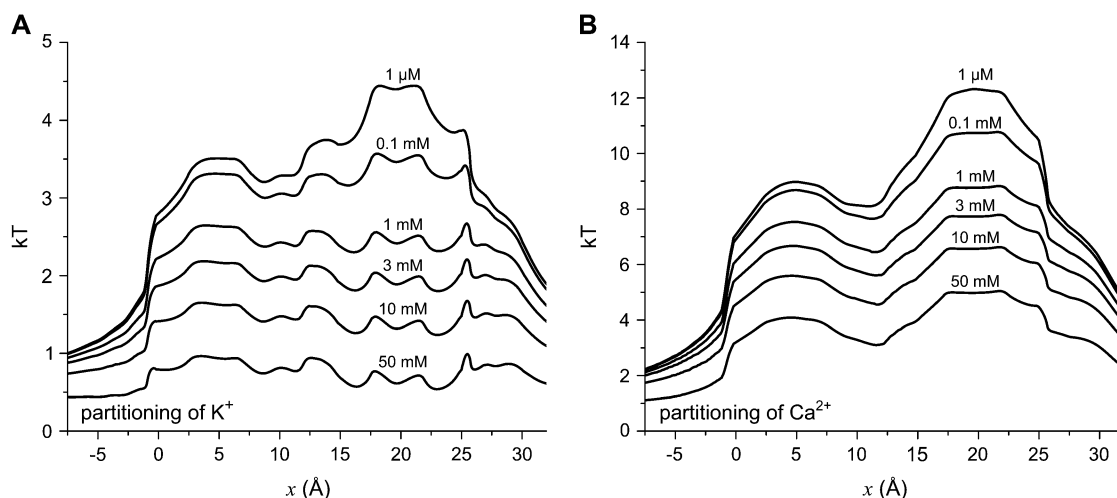


FIGURE 3 The partitioning coefficient of  $\text{K}^+$  (A) and  $\text{Ca}^{2+}$  (B) plotted logarithmically.  $[\text{K}^+] = 150$  mM and the indicated  $[\text{Ca}^{2+}]$  is in both baths.

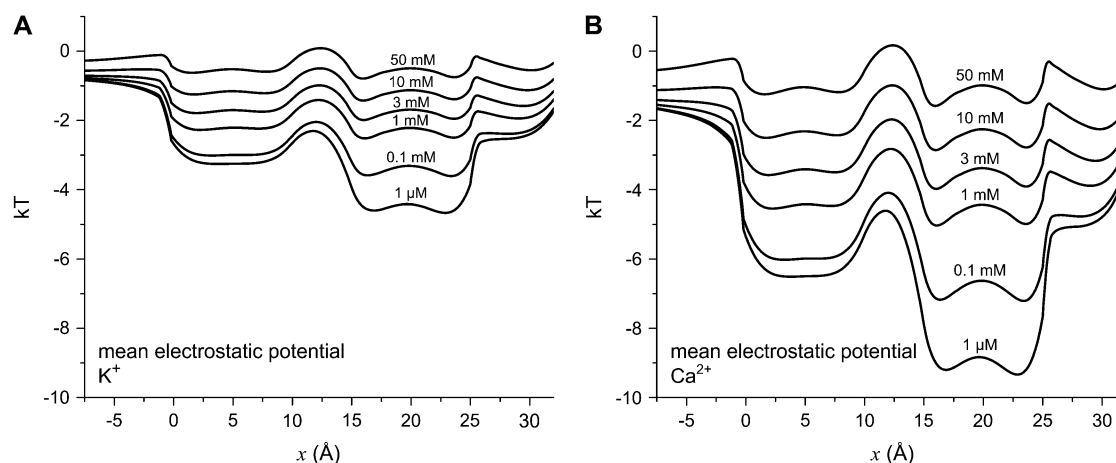


FIGURE 4 The electrostatic component of partitioning  $z_i e \phi(x)/kT$  of  $K^+$  (A) and  $Ca^{2+}$  (B) in the pore.  $[K^+] = 150$  mM and the indicated  $[Ca^{2+}]$  is in both baths.

Here, the binding selectivity is defined by the ratio of the ion concentrations in the pore and by Eqs. 2 and 7 is naturally decomposed into four energetic advantages, energy differences that each favor the binding of one ion species over the other. In this case, a positive term favors the binding of  $Ca^{2+}$  while a negative term favors  $K^+$ .

It is more convenient to describe the energetics of binding selectivity with a single number rather than an entire profile (like in Figs. 3–6), and so only the relative concentrations of  $Ca^{2+}$  and  $K^+$  in Eq. 8 in the middle of the Asp-4899 region (i.e., at  $x = 20$  Å) are considered. This location is chosen because it is representative of the changes in general, as well as being the location where ion concentrations are highest and ion selectivity occurs.

All the terms of Eq. 8 are shown in Fig. 7 for  $[Ca^{2+}]$  ranging from 1  $\mu$ M to 50 mM. As  $[Ca^{2+}]$  increases, the

overall binding selectivity of  $Ca^{2+}$  increases (solid line). This displacement of  $K^+$  by  $Ca^{2+}$  is determined by how each of the terms in Eq. 8 changes as  $[Ca^{2+}]$  increases:

1. Number advantage (Fig. 7, horizontal-hatched column). The only term that favors  $K^+$  binding in the pore is its number advantage; there is more  $K^+$  in the baths than  $Ca^{2+}$  and therefore it is more probable that a  $K^+$  ion enters the channel. Even this advantage is overcome by the electrostatic and excluded-volume terms at just 0.1 mM  $CaCl_2$  in the bath.
2. Mean electrostatic advantage (Fig. 7, diagonal-hatched column). The mean electrostatic potential inside the pore always favors  $Ca^{2+}$ , but it reduces to almost zero as  $[Ca^{2+}]$  becomes comparable to  $[K^+]$  (see also Fig. 4). The long-ranged average electrostatic potential only attracts  $Ca^{2+}$  to the pore when  $[Ca^{2+}]$  is low.

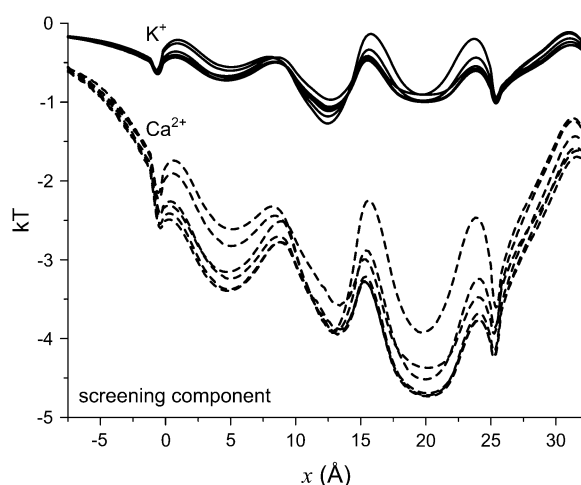


FIGURE 5 The screening component of partitioning  $\mu_i^{SC}(x)/kT$  of  $K^+$  (solid lines) and  $Ca^{2+}$  (dashed lines) in the pore.  $[K^+] = 150$  mM and  $[Ca^{2+}]$  is changed from 1  $\mu$ M to 50 mM. Because the curves are so close together,  $[Ca^{2+}]$  is not indicated.

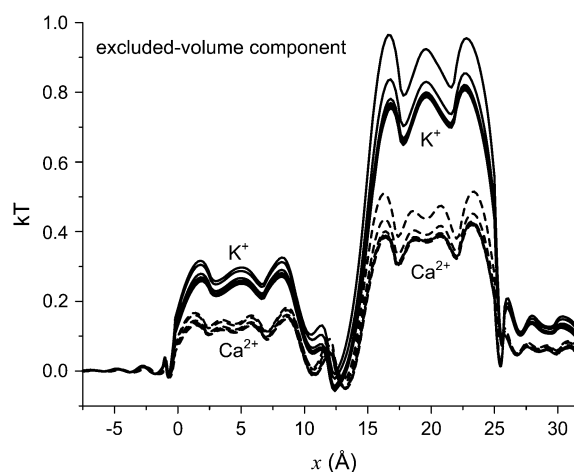


FIGURE 6 The excluded-volume (hard-sphere) component of partitioning  $\Delta\mu_i^{HS}(x)/kT$  of  $K^+$  (solid lines) and  $Ca^{2+}$  (dashed lines) in the pore.  $[K^+] = 150$  mM and  $[Ca^{2+}]$  is changed from 1  $\mu$ M to 50 mM. Because the curves are so close together,  $[Ca^{2+}]$  is not indicated.

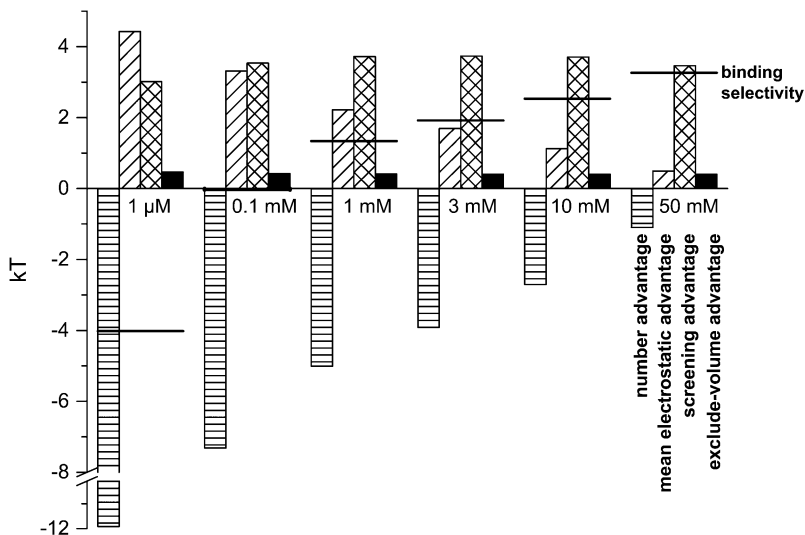


FIGURE 7 Components of the binding selectivity from Eq. 8 in the selectivity filter at  $x = 20$  Å in Fig. 1.  $[K^+] = 150$  mM and the indicated  $[Ca^{2+}]$  is in both baths. The horizontal-hatched bar is the number advantage, the diagonal-hatched bar is the mean electrostatic advantage, the cross-hatched bar is the screening advantage, and the solid bar is the excluded-volume advantage. The horizontal line is the binding selectivity of Eq. 8 (i.e., the sum of all the terms). A positive term favors the binding of  $Ca^{2+}$  while a negative term favors  $K^+$ .

3. Screening advantage (Fig. 7, *cross-hatched column*). When  $[Ca^{2+}]$  is higher than  $\sim 0.1$  mM, then the largest term favoring  $Ca^{2+}$  binding in the pore is the screening advantage of  $Ca^{2+}$ . Fig. 5 showed that the screening term of  $Ca^{2+}$  in the selectivity filter was  $\sim -4.5$  kT while for  $K^+$  it was only  $\sim -1$  kT; the large difference in these terms is the 3.5 kT screening advantage for  $Ca^{2+}$  shown in Fig. 7. Most importantly, this screening advantage is unchanged as  $[Ca^{2+}]$  is increased to provide the largest energetic preference for  $Ca^{2+}$  over  $K^+$  (and over other monovalent cations as described below). While the excluded-volume advantage of  $Ca^{2+}$  is also unchanged, that term is much smaller (see below).
4. Excluded-volume advantage (Fig. 7, *solid column*). This term is also unchanged as  $[Ca^{2+}]$  is increased, but at  $\sim 0.5$  kT it is generally the smallest term favoring  $Ca^{2+}$  binding in the pore. Because  $Ca^{2+}$  ions are smaller than  $K^+$  ions (diameters of 2 Å versus 2.76 Å, respectively), it is easier to insert a  $Ca^{2+}$  ion into the crowded pore than a  $K^+$  ion. While the excluded-volume advantage of  $Ca^{2+}$  is generally small, this term does have a significant effect on  $Ca^{2+}$  versus monovalent selectivity as described below.

Combining these results, it is clear that the origin of the  $Ca^{2+}$  selectivity of RyR is electrostatics; the sum of the mean electrostatic and screening advantages is enough to overcome the large number advantage of  $K^+$ . However, the average electrostatic attraction of the  $Ca^{2+}$  ions from any net charge in the selectivity filter is not solely responsible for the selectivity. While a  $Ca^{2+}$  ion always “feels” twice the electrostatic pull that a  $K^+$  ion does because of its two positive charges, the net charge throughout the pore is close to zero in the pore as  $[Ca^{2+}]$  increases above 10 mM (Fig. 7); that is, there is little electrostatic pull on the cations (on average) to move into the pore at high  $[Ca^{2+}]$ . When  $[Ca^{2+}]$  becomes comparable to  $[K^+]$  it is only the superior ability of

the  $Ca^{2+}$  to screen the protein charges that favors  $Ca^{2+}$  accumulation in the pore because all other terms are small in comparison. The number advantage is also an important term. When  $[Ca^{2+}]$  is  $< \sim 3$  mM  $Ca^{2+}$  (the physiological upper limit in the sarcoplasmic reticulum) it is larger than any other single term. Moreover, when considering the L-type  $Ca^{2+}$  channel that has a  $Ca^{2+}$  affinity of 1 μM, the monovalent number advantage is a whopping 12 kT that must be overcome by the other terms.

### Role of monovalent size in $Ca^{2+}$ versus monovalent cation selectivity

In vivo, RyR must select  $Ca^{2+}$  ions from a background of  $K^+$  ions, but in vitro, many different kinds of cations can be used. An important check for any theory that reproduces the  $Ca^{2+}$  versus  $K^+$  selectivity is to use the same pore model to reproduce the selectivity data of different monovalent cations. The model of RyR described here does this. Besides Figs. S1–S9 shown in the Supplementary Material, Fig. 2 shows that the model can predict measurable differences in the selectivity of  $Ca^{2+}$  versus  $Na^+$  and  $Ca^{2+}$  versus  $Cs^+$ . These two monovalents were chosen because they have similar conductances through RyR, and therefore any differences are mainly due to their size difference ( $Na^+$  and  $Cs^+$  diameters are 2 Å and 3.4 Å, respectively (54)).

The significant changes that occur when different monovalent cations compete with  $Ca^{2+}$  for the pore can be seen in Fig. 8. In this figure, the concentration profiles of the monovalents and  $Ca^{2+}$  in the pore are shown for  $[X^+] = 150$  mM ( $X^+ = Li^+, Na^+, K^+$ , and  $Cs^+$ , listed from smallest to largest) and  $[Ca^{2+}] = 1$  mM. As monovalent diameter increases from 1.33 Å for  $Li^+$  to 3.4 Å for  $Cs^+$ , the monovalent concentration throughout the pore decreases and the  $Ca^{2+}$  concentration increases. Within the selectivity filter itself, there is a  $>80\%$  decrease in monovalent concentration ( $Cs^+$  versus  $Li^+$ ) and a 40% increase in  $Ca^{2+}$  concentration.

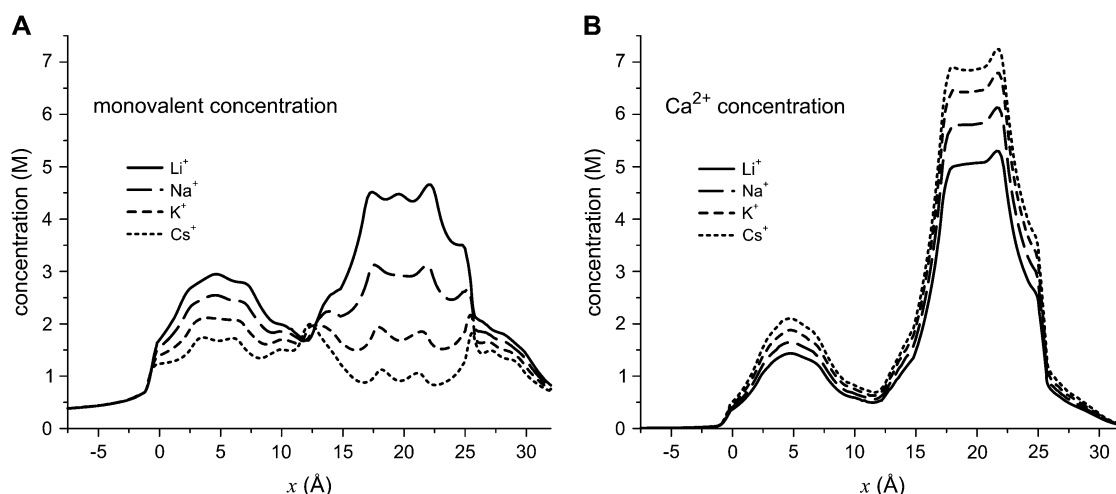


FIGURE 8 Concentration profiles in the pore of the monovalent cation (A) and  $\text{Ca}^{2+}$  (B). For each indicated monovalent cation  $\text{X}^+$ ,  $[\text{X}^+] = 150$  mM and  $[\text{Ca}^{2+}] = 1$  mM in both baths.

To understand this substantial change, Fig. 9 shows the chemical potential decomposition of Eq. 8 for different monovalents:

1. Number advantage (Fig. 9, *horizontal-hatched column*). This term is constant since  $[\text{Ca}^{2+}]$  and  $[\text{X}^+]$  are constant.
2. Mean electrostatic advantage (Fig. 9, *diagonal-hatched column*). All of the monovalents create the same mean electrostatic potential inside the selectivity filter and therefore this advantage for  $\text{Ca}^{2+}$  accumulation is constant.
3. Screening advantage (Fig. 9, *cross-hatched column*).  $\text{Ca}^{2+}$  still has a screening advantage because of its higher valence. The relative screening between two cations in the pore is not just a function of the valence, however. The relative size of the ions is also important. This can be seen from the analytic formulas of the mean spherical

approximation for homogeneous electrolytes (14,31,35). Because of this, the screening advantage for  $\text{Ca}^{2+}$  is  $\sim 0.5$  kT smaller when competing against  $\text{Li}^+$  and when competing against  $\text{Cs}^+$ .

4. Excluded-volume advantage (Fig. 9, *solid column*). This term favors the smaller ion. Since  $\text{Li}^+$  is the only monovalent considered that is smaller than  $\text{Ca}^{2+}$ , it is the only one with an excluded-volume advantage (albeit a very small one at  $\sim 0.25$  kT).  $\text{Ca}^{2+}$ , however, has a relatively large excluded-volume advantage over  $\text{Cs}^+$  of  $\sim 1$  kT.

Combining these results, it is the number and mean electrostatic terms that remain constant as monovalent size is changed; previously, when  $[\text{Ca}^{2+}]$  was changed, these terms changed substantially. Vice versa, the screening and excluded-

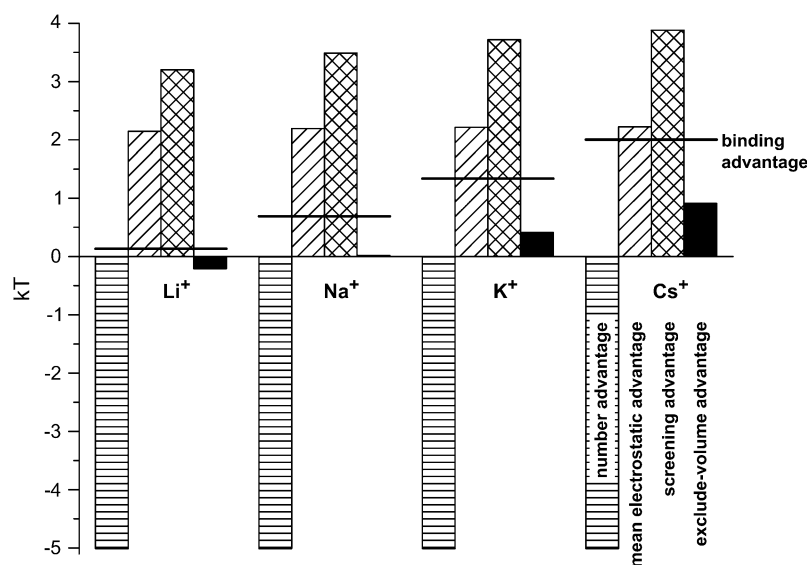


FIGURE 9 Components of the binding selectivity from Eq. 8 in the selectivity filter at  $x = 20$  Å in Fig. 1. For each indicated monovalent cation  $\text{X}^+$ ,  $[\text{X}^+] = 150$  mM and  $[\text{Ca}^{2+}] = 1$  mM in both baths. Ion diameters:  $\text{Li}^+$  1.33 Å;  $\text{Na}^+$  2.00 Å;  $\text{K}^+$  2.76 Å; and  $\text{Cs}^+$  3.40 Å. The horizontal-hatched bar is the number advantage, the diagonal-hatched bar is the mean electrostatic advantage, the cross-hatched bar is the screening advantage, and the solid bar is the excluded-volume advantage. The horizontal line is the binding selectivity of Eq. 8 (i.e., the sum of all the terms). A positive term favors the binding of  $\text{Ca}^{2+}$  while a negative term favors the monovalent.



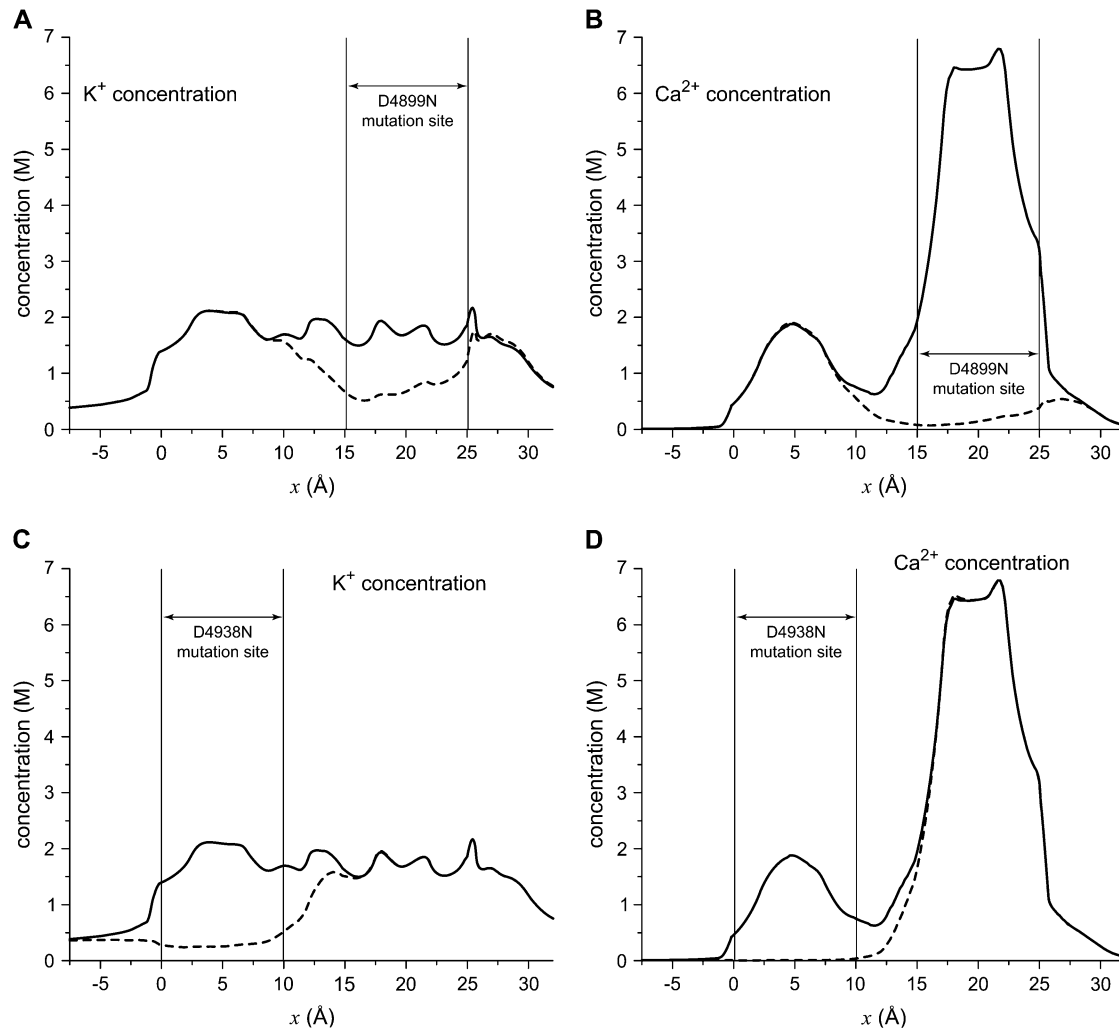


FIGURE 10 Concentration profiles in the pore for the mutations D4899N (A and B) and D4938N (C and D) for  $K^+$  (A and C) and  $Ca^{2+}$  (B and D). The profiles for native (WT) channel are the solid lines and for the mutations the dashed lines.  $[K^+] = 150$  mM and  $[Ca^{2+}] = 1$  mM in both baths. In the model, the mutation is created by “turning off” the charge on the four Asp-4899s or the four Asp-4939s. The mutation site is the region from which the charge has been removed.

volume terms that remained approximately constant as  $[Ca^{2+}]$  varied now change as monovalent size is varied. These two terms combined only change  $\sim 1.75$  kT, but this is enough to change the relative concentrations of  $Ca^{2+}$  and monovalent in the selectivity filter from  $\sim 1:1$  for  $Ca^{2+}$  versus  $Li^+$  to  $>7:1$   $Ca^{2+}$  versus  $Cs^+$  (Fig. 8). The excluded-volume term is the one that changes the most. Therefore, is the most significant factor in determining the amount of  $Ca^{2+}$  versus monovalent selectivity, even though it is generally  $<1$  kT in magnitude.

### Effects of mutations on $Ca^{2+}$ versus $K^+$ selectivity

The model of RyR permeation and selectivity described here correctly reproduces and predicts the  $Ca^{2+}$  versus monovalent cation selectivity. Without adjusting any parameters, the model also reproduces the experimentally measured decrease

in conductance and selectivity when specific charged amino acids are mutated to neutral analogs. These include the mutations D4899N, E4900Q, and D4938N (see Supplementary Material). In the model, these mutations are produced by changing the charge on these amino acids to zero; no other parameters (e.g., diffusion coefficients, pore radius) are changed.

Here, two of these mutations are considered in detail: D4899N and D4938N. Each results in a significant reduction of  $Ca^{2+}$  versus  $K^+$  selectivity; D4899N reduces the permeability ratio  $P_{Ca}/P_K$  from a native wild-type (WT) value of 7.0 to 3.4 and D4839N reduces it to 3.3 (7,43). This loss of selectivity is reflected in the cation profiles shown in Fig. 10. In both cases, there is a significant reduction in both  $Ca^{2+}$  and  $K^+$  in the region where the mutation occurred (indicated by the vertical lines) and a neighboring region. In other parts of the pore, the profiles are virtually identical to the native

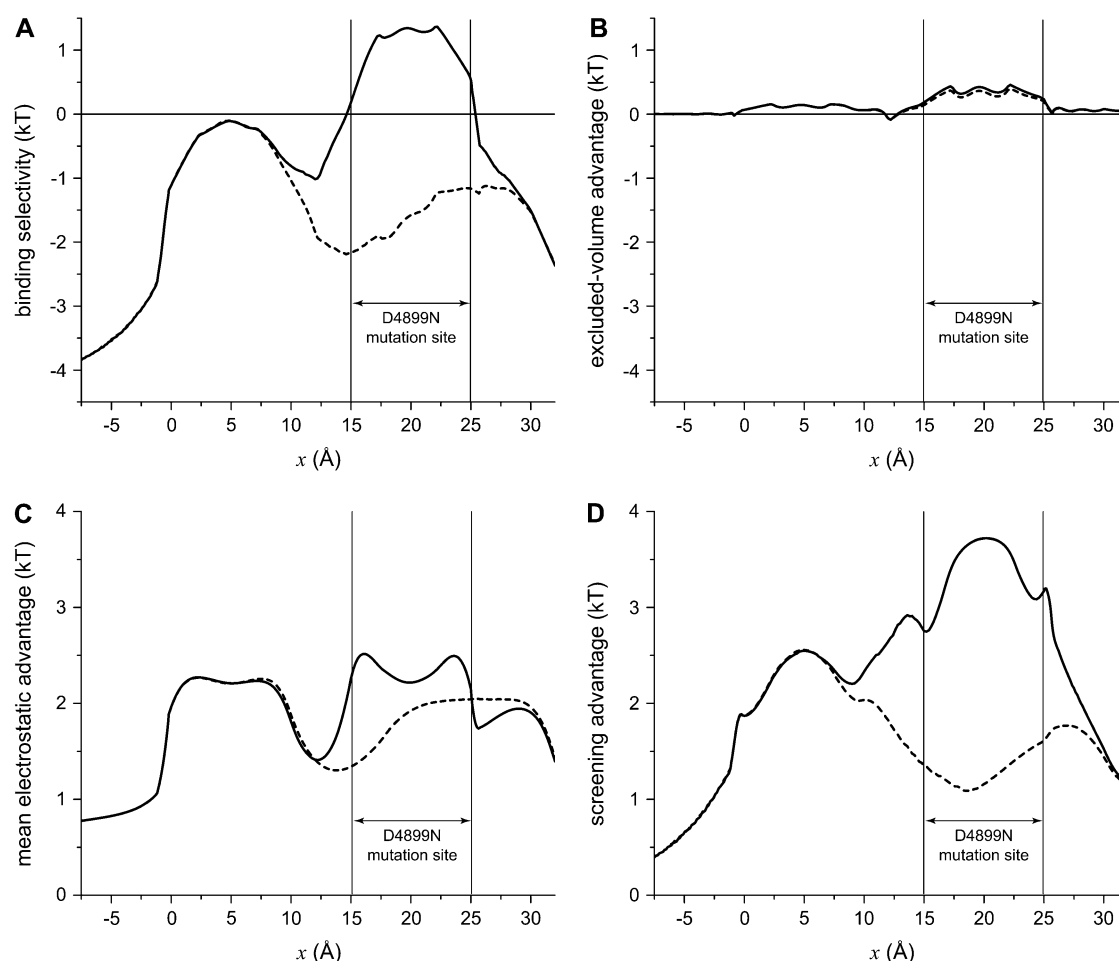


FIGURE 11 Profiles of the binding selectivity from Eq. 8 (A) and its components (excluded volume, B; mean electrostatic, C; screening, D) for the native (WT) channel (solid line) and the mutation D4899N (dashed line). The conditions are those described in Fig. 10.

profiles. The changes are very localized, but the resulting large changes in the current/voltage curves (see Supplementary Material) show that these localized changes in the cation profiles have significant and important measurable effects.

To understand the differences in binding selectivity in these mutations compared to native RyR, the same chemical potential decomposition of Eq. 8 can be used. In this case, however, it is more instructive to consider the entire profile through the pore rather than just a single location. Figs. 11 and 12 show the energetics for D4899N and D4938N (dashed lines), respectively, compared to native RyR (solid lines). In both cases, there is a significant ( $\sim 3$  kT) loss of  $\text{Ca}^{2+}$  binding compared to  $\text{K}^+$  in the mutated region (Fig. 11 A and Fig. 12 A). In the regions neighboring the mutation site—up to  $7.5$  Å away—there is also significant loss of  $\text{Ca}^{2+}$  binding; each mutation has far-reaching effects. Analyzing the chemical potential components again gives insight into why this occurs:

1. Excluded-volume advantage (Fig. 11 B and Fig. 12 B). This term does not change significantly in the mutant RyRs.

2. Mean electrostatic advantage (Fig. 11 C and Fig. 12 C). Zeroing the charge in a region of the pore is expected to change the mean electrostatic potential in that region, and it does. But in the two mutations, the results are different. In D4899N, the region where the mean electrostatic potential differs from native profile by more than  $1$  kT is small compared to D4938N (compare Fig. 11 C and Fig. 12 C). For D4938N, the entire mutation site as well as a neighboring region has a mean electrostatic potential difference (compared to native) of  $\sim 1.5$  kT. In both mutations, the change in this potential is localized to the mutation site and  $\sim 2.5$  Å on either side; in the rest of the pore the potential is the same as in native RyR.
3. Screening advantage (Fig. 11 D and Fig. 12 D). The largest change is a reduction in the screening advantage of  $\text{Ca}^{2+}$  in and around both mutation sites. This change—up to  $2$  kT—extends up to  $7.5$  Å away from the mutation sites.

Altogether, the charge-deletion mutations result in an environment with significantly smaller mean electrostatic and

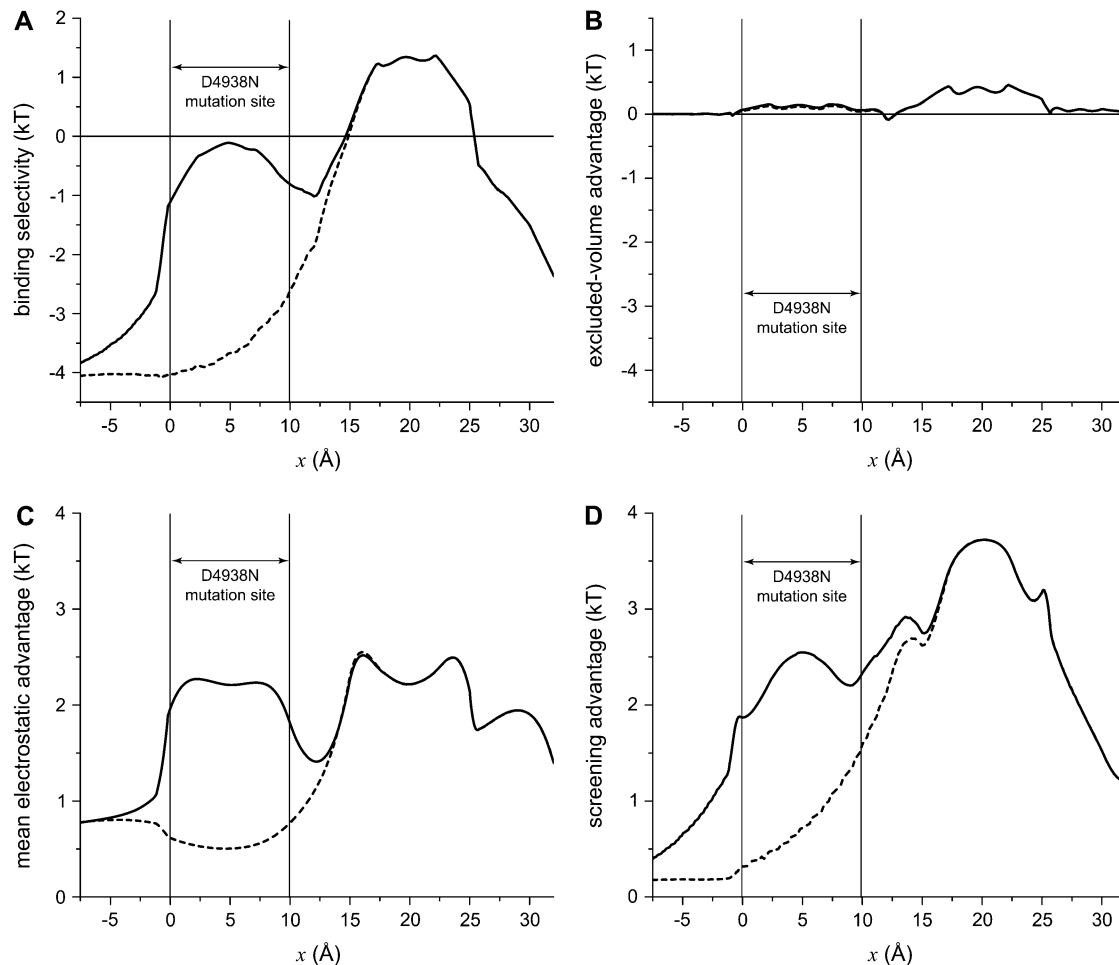


FIGURE 12 Profiles of the binding selectivity from Eq. 8 (*A*) and its components (excluded volume, *B*; mean electrostatic, *C*; screening, *D*) for the native (WT) channel (*solid line*) and the mutation D4938N (*dashed line*). The conditions are those described in Fig. 10.

screening advantages of  $\text{Ca}^{2+}$  over  $\text{K}^{+}$ ;  $\text{Ca}^{2+}$  retains some advantage, but in each case up to 2 kT less than in native RyR. Because electrostatic correlations range over the local screening (Debye) length (22,34), changes in the mutation site produce changes in the ionic concentration a distance away. Both  $\text{Ca}^{2+}$  and  $\text{K}^{+}$  concentrations are reduced and because of the loss of up to 4 kT between these two electrostatic advantages, the  $\text{K}^{+}$  concentration is now significantly higher than that of  $\text{Ca}^{2+}$ ; the ratio of  $\text{K}^{+}$  concentration to  $\text{Ca}^{2+}$  concentration is less than 1 in the mutants so the dashed lines in Fig. 11 *A* and Fig. 12 *A* are  $<0$ .

## DISCUSSION

In equilibrium, the energetics of  $\text{Ca}^{2+}$  versus monovalent cation binding selectivity in the pore RyR can be decomposed into the four terms in Eq. 8: 1), the number advantage that describes which ion species has a larger concentration in the baths; 2), the mean electrostatic advantage that describes the average electrostatic well/barrier in the channel due to the

long-time average local net charge (through the Poisson equation); 3), the screening advantage that describes the ability of an ion to electrostatically coordinate with other ions within a screening (Debye) length on the atomic timescale; and 4), the excluded-volume advantage that, in this article, describes the effect of hard-sphere ions not being able to overlap.

Each of the four chemical potential terms plays an important role in  $\text{Ca}^{2+}$  versus monovalent cation selectivity, as detailed now.

## Number advantage

In calcium-selective channels, the number advantage that monovalents generally have over divalents is the challenge that selectivity must overcome; all other energies must overcome the number advantage. For example, in the physiological conditions in the sarcoplasmic reticulum encountered by RyR,  $[\text{Ca}^{2+}]$  is  $\sim 1$  mM while  $[\text{K}^{+}]$  is  $\sim 150$  mM—a number advantage equivalent to 5 kT of

chemical potential in favor of  $K^+$ . Moreover, in experiments (e.g., on the L-type calcium channel or in Fig. 2)  $[Ca^{2+}]$  can be 1  $\mu M$  (or less)—a number advantage of 12 kT (or more) in favor of the monovalent.

In RyR, when the number advantage for  $K^+$  is removed by increasing  $[Ca^{2+}]$ , the mean electrostatic potential throughout the pore goes to zero as more  $Ca^{2+}$  enters (Fig. 4) and  $K^+$  is displaced (Fig. 3 A). Recent work using grand canonical Monte Carlo simulations has shown that this displacement of  $K^+$  is a nonlinear function of the environment in the pore and how important it is to do all calculations at the experimental  $[Ca^{2+}]$  (11,12,55). While simulation results from 18 mM  $Ca^{2+}$  have been extrapolated down to 1  $\mu M$   $Ca^{2+}$  by Corry et al. (15), a theory is required to do this. Without further simulations, however, it is impossible to verify the theory or its assumptions. Ideally, a theory like PNP/DFT that spans all concentration ranges should be applied. Since PNP/DFT directly computes the average thermodynamic quantities and does not simulate particle trajectories, bath concentrations are just input parameters for the theory.

## Electrostatics

In total, the electrostatics of the system are the major driving force for  $Ca^{2+}$  versus monovalent selectivity, in general agreement with Corry et al. (15,16). However, since DFT naturally decomposes the electrostatics into the two physically distinct mean electrostatic and screening terms (see Theory and Methods), the PNP/DFT approach can give a more thorough understanding of how the electrostatics contributes to selectivity. With 150 mM  $K^+$  in the bath, the screening advantage of  $Ca^{2+}$  is always more than the mean electrostatic advantage if  $[Ca^{2+}]$  is  $>0.1$  mM (Fig. 7). Moreover, the mean electrostatic advantage disappears as  $[Ca^{2+}]$  is increased while the screening advantage remains largely unchanged (Fig. 7). Therefore, it is the screening advantage of  $Ca^{2+}$  that is the dominant electrostatic term.

Ionic screening is a reflection of an ion's ability to coordinate with neighboring ions and thereby lower the system's energy. This coordination is a function of both the ion's charge and size (as well as the other ions' charges and sizes) and is a balance of electrostatic and excluded-volume forces (14,31,34); it is even possible that a small monovalent ion can screen better than a large divalent (40,56). It is not, however, possible to explain this term just with the mean-field Poisson equation and the excluded volume components. The mean electrostatic potential ignores the local inhomogeneities of the fluid because it includes only the average concentration of the charges; for example, it does not "know" whether there is a liquid or a perfect crystal. In fluids, this local structure can be described by the DFT used here with the screening and excluded-volume components of the chemical potential.

As a local balance of electrostatic and excluded-volume forces, an ion species' screening advantage then directly

reflects the CSC mechanism of selectivity; the excluded-volume term reflects another component. This is especially true for  $Ca^{2+}$  because its screening advantage over monovalent cations is large ( $\sim 4$  kT), indicating that  $Ca^{2+}$  coordinates significantly better, especially in the crowded environment of the selectivity filter (Fig. 7). In other words, the large screening advantage of  $Ca^{2+}$  shows that  $Ca^{2+}$  can more efficiently balance the negative charges of the protein (e.g., Asp-4899 in the selectivity filter) than the monovalents.

## Excluded volume

While the electrostatic terms are generally the largest, the excluded-volume (hard-sphere) term is generally the smallest—but still important in selectivity. If electrostatics were purely responsible for  $Ca^{2+}$  versus monovalent selectivity, then there would be little difference in the concentration of  $Ca^{2+}$  and different monovalent cations in the selectivity filter. The calculations, however, show a large difference (Fig. 8); there is significantly less  $Ca^{2+}$  in the pore with the small  $Li^+$  (1.33 Å diameter) as the monovalent than with the large  $Cs^+$  (3.4 Å diameter). The chemical potential decomposition done in the DFT (Fig. 9) demonstrates that this difference is due to changes in both the screening (up to  $\sim 0.5$  kT) and excluded-volume terms (up to  $\sim 1$  kT). The larger the monovalent, the more both terms favor  $Ca^{2+}$  binding.

This trend reflects the CSC selectivity mechanism: it is the small ions (e.g.,  $Li^+$  and  $Ca^{2+}$ ) that can more efficiently balance the protein charges than the large ions (e.g.,  $Cs^+$ ) because they occupy less space in the crowded selectivity filter. Fig. 8 shows this in terms of ion concentrations in the pore. If  $Cs^+$  is replaced by  $Li^+$  as the monovalent, then  $Ca^{2+}$  concentration in the selectivity filter decreases  $\sim 30\%$  while monovalent concentration increases  $\sim 500\%$  (compare *dotted* and *solid lines* in Fig. 8). The small  $Li^+$  takes up only 6% of the volume of the large  $Cs^+$  and therefore fits more easily into the selectivity filter.  $Ca^{2+}$  is displaced because more monovalents are in the filter to balance the negative Asp-4899 protein charges. The exact ratio of  $Ca^{2+}$  to monovalent concentration in the pore is a balance of the electrostatic and excluded-volume forces—charge/space competition.

It is important to note that, while changes in the excluded-volume advantage are relatively small at  $\sim 1$  kT or less, the ion concentrations in the pore depend on all the terms exponentially (Eq. 6); small changes in any term can have a large effect. It is because of this that any model must reproduce experimental data over a wide range of conditions. Only then can one have confidence that the energies in the model change correctly as conditions are changed. For this reason, all the data reproduced by the model—more than 100 different ionic solutions—are shown in this article. Specifically, Figs. 2 and S9 show that the PNP/DFT model correctly reproduces RyR's  $Ca^{2+}$  versus monovalent affinity as  $[Ca^{2+}]$  is changed.

## Flexible coordination in the selectivity filter

The balance of electrostatics and excluded volume in the selectivity filter that is the CSC mechanism of selectivity is consistent with a more general idea of selectivity that is emerging from the study of other ion channels. In the potassium channel, Noskov and Roux (57) and Varma and Rempe (58) describe how the carbonyl oxygens in that selectivity filter form an environment that best coordinates  $K^+$ . In the sodium channel, Boda et al. (55) show how the amino acids of the DEKA locus arrange around the permeant ions, with  $Na^+$  being coordinated best compared to  $K^+$  and  $Ca^{2+}$ . In those channels and in the calcium channels studied previously with Monte Carlo simulations (8–12,59), the channel protein forms a flexible environment that coordinates the “correct” ion better than the other ions, leading to binding selectivity.

The situation is the same for RyR with the carboxyl groups of the DDDD locus (from Asp-4899) coordinating  $Ca^{2+}$  best among the permeant ions. This is quantified by the screening and excluded-volume advantages of  $Ca^{2+}$ . Both of these terms indicate how well an ion “fits into” the crowded environment of the selectivity filter, either by its ability to coordinate with (screen) neighboring ions and protein charges (the screening advantage) or by its ability to find space among the other atoms (the excluded-volume advantage). In the L-type calcium channel, Nonner and Eisenberg found screening and excluded-volume terms of similar size both by adding excess chemical potentials as fitting parameters into PNP (13) and by modeling the pore contents as a fluid with the mean spherical approximation (14). Because the L-type channel is more narrow than RyR (60), the concentrations were higher in that work, resulting in slightly more positive excluded-volume terms and more negative screening terms. These differences reproduced the micro-molar  $Ca^{2+}$  affinity of the L-type channel.

The same balance of electrostatics and excluded volume has also been noted in other proteins. For example, cation binding in the EF-hand loops of calmodulin has been found to be a balance of the cation’s charge and size as well as the flexibility of the loops (61). The EF-hand motif is a common calcium binding site motif rich in aspartates, glutamates, and asparagines, making the amino-acid structure very similar to calcium channel selectivity filters.

## CONCLUSION

A PNP/DFT model was used to analyze the energetics of equilibrium binding selectivity in RyR. The extension of a previous model (20) presented here uses nine data points to determine model parameters that were then never changed. The model reproduces both native and mutant RyR permeation and selectivity data in over 100 different ionic solutions and predicted the presence of different sized AMFEs when  $Ca^{2+}$  was added to  $Na^+$  and when  $Ca^{2+}$  was added to  $Cs^+$ . It had previously predicted an AMFE for mixtures of  $Na^+$  and

$Cs^+$  (20). While there are approximations in the model that need to be explored further (e.g., no dehydration/resolution penalty for ions moving from the bath into the pore), the PNP/DFT approach has advantages over other methods including fast computing time (minutes for an entire current/voltage curve) and arbitrarily small bath concentrations.

The model shows that  $Ca^{2+}$  versus monovalent cation selectivity in RyR is determined by the CSC mechanism that balances the electrostatic attraction of the negative protein charges (especially Asp-4899) with the excluded volume of the ions and protein charges in the selectivity filter. This balance in favor of  $Ca^{2+}$  is achieved by having a selectivity filter that contains negatively-charged carboxyl groups on tethers so they are free to move in response to the permeant ions currently in the filter and by thermal motion. In this sense, the CSC mechanism is consistent with the selectivity by the flexible coordination provided by the channel protein seen in other channels and proteins (55,57,58,61).

## APPENDIX: CONSTRUCTING THE MODEL

The model of ion permeation through the open RyR channel is a refinement of the model described in Gillespie et al. (20) that includes new mutation data (43) that was not available when the first model was created. Specifically, two charge-neutralizing mutations of aspartates in the cytosolic (*cis*) vestibule of the pore (D4938N and D4945N) were shown to affect RyR conductance and selectivity: the conductances in 250 mM symmetric KCl were 65% and 92% of WT for D4938N and D4945N, respectively, and permeability ratios  $P_{Ca}/P_K$  were reduced from 7.0 to 3.3 and 6.5. Charge-neutralizing mutations (D or E to N or Q) of other charged amino acids in the cytosolic vestibule did not affect either  $K^+$  conductance or  $Ca^{2+}$  versus  $K^+$  selectivity (43).

Previous experiments (7,42) showed that neutralizing the charge on two negatively-charged amino acids (Asp-4899 and Glu-4900) significantly reduced both conductance and selectivity: the conductances in 250 mM symmetric KCl were 20% and 56% of WT for D4899N and E4900Q, respectively, and permeability ratios  $P_{Ca}/P_K$  were reduced from 7.0 to 3.4 and 3.2. Except for the mutation E4902Q, charge-neutralizing mutations of other charged amino acids in the luminal vestibule did not affect either  $K^+$  conductance or  $Ca^{2+}$  versus  $K^+$  selectivity. While the conductance of E4902Q was found to be similar to WT, a small but statistically significant change from WT in  $Ca^{2+}$  selectivity was found (42) so E4902 was also included in this model.

Only Asp-4899 and Glu-4900 were explicitly included in the first model of RyR (20), although a region of negative charge in the cytosolic vestibule was required to reproduce the data. In hindsight, these were the then-unknown Asp-4938 and Asp-4945. In the model described here, all of the charged amino acids found in mutation experiments to affect RyR conductance and selectivity (while still producing functional and caffeine- and ryanodine-sensitive channels) were included: Asp-4899 in the selectivity filter, Asp-4938 and Asp-4945 in the cytosolic vestibule, and Glu-4900 and Glu-4902 in the luminal vestibule (Fig. 1).

Since no high-resolution structures of the RyR are available, it was necessary to reverse-engineer the location of these amino acids. Several low-resolution electron microscopy structures of the entire RyR protein in the closed state that were published after the initial model were used to guide this revision of the model pore (62,63). Construction of the model pore was done in a way similar to that described in Gillespie et al. (20), but the basic method is outlined here. Because of the homology between RyR and the potassium channel (63), the pore was given a narrow selectivity filter with a wider cytosolic vestibule. The selectivity filter radius was chosen to be the same as in the previous model (4 Å), and 15 Å in length. Homology models

derived from low-resolution structures of the RyR pore indicate that the selectivity filter includes residues 4894–4899 (GGGIGD) (62). The model selectivity filter is long enough to include these amino acids, but only Asp-4899 is explicitly modeled (Fig. 1). The cytosolic vestibule radius was chosen to be 7 Å, consistent with low-resolution RyR structures (M. Samsó, Harvard Medical School, personal communication, 2007), although the model cannot distinguish between different vestibule radii as it can between different selectivity filter radii (Fig. 15 of (20)).

As in the previous model, Glu-4900 was placed at the selectivity filter/luminal vestibule junction. Glu-4902 was placed on the luminal face of the channel. These are in accordance with other modeling of the RyR pore based on KcsA homology and mutation experiments (Fig. 2 of (42)). Asp-4938 was placed in the cytosolic vestibule in accordance with homology modeling from low-resolution RyR structures and 15 Å away from Asp-4899 (62). Asp-4945 was placed 10 Å away from Asp-4938 toward the cytosolic end of the pore (62,63) because, as part of the same  $\alpha$ -helix, they are approximately two helix-turns apart. Because the structure of the RyR pore in the open state has not yet been determined at a resolution sufficient to distinguish the conformation of the inner helices, the increase in pore radius near Asp-4945 was arbitrarily chosen to be 45°. The model is not sensitive enough to distinguish between different helix-tilt angles.

Each of the aspartates and glutamates were assumed to be fully charged and facing into the permeation pathway with the terminal carboxyl ( $\text{COO}^-$ ) group on a flexible tether that can span a hemisphere of radius 5 Å for aspartates and 7 Å for glutamates (Fig. 1). In the one-dimensional Poisson-Nernst-Planck/Density functional theory (PNP/DFT) model (13,20), residues Asp-4938, Asp-4899, and Glu-4900 were modeled as two independent, half-charged oxygen ions (2.8 Å diameter) confined to a region of the long axis of the pore spanned by each residue's hemisphere (8,11,12,14,20). For example, the centers of the oxygens for Asp-4899 were confined to  $15 \text{ Å} < x < 25 \text{ Å}$  in Fig. 1. The other residues in the model (Asp-4945 and Glu-4902) were modeled as regions of uniform fixed charge (i.e., just a background charge and not as ions that take up space) because the pore radius where they were located was too wide for the residues to exert excluded-volume effects on the permeating ions; their presence was only felt electrostatically by the permeating ions.

Many important structural inferences were made from the first model (20) that have not changed in this model (e.g., selectivity filter radius of 4 Å and the location of Glu-4900 at the selectivity filter/luminal vestibule interface and that its range of tethered movement overlapped with that of Asp-4899). Other structural parameters were constrained by known structural information (e.g., distance of Asp-4938 from Asp-4899 or distance of Asp-4945 from Asp-4938) or were chosen to have a reasonable value (e.g., range of tethered movement of side chains, location of Glu-4902, or pore radius in the cytosolic vestibule). The results were insensitive to the exact choice of these latter values. Given the constraints of the previous model and known structural information and the insensitivity of the other parameters, there were no adjustable parameters with respect to the structure in this model.

There were, however, some parameters for the ions that had to be determined from the experimental data: the diffusion coefficients of the permeating ions and water are inputs to the PNP/DFT model. Because water does not contribute to the current and  $\text{Cl}^-$  does not permeate the channel, these were given diffusion coefficients of 1% of bulk within the pore. Previously it was shown that the results of the model did not change even when bulk diffusion coefficients were used (20). For the cations, three different diffusion coefficients were used within the pore, one in each of the following regions: in the cytosolic vestibule where Asp-4938 was confined ( $0 \text{ Å} < x < 10 \text{ Å}$ ), in the selectivity filter ( $10 \text{ Å} < x < 25 \text{ Å}$ ), and in the luminal vestibule ( $25 \text{ Å} < x < 32 \text{ Å}$ ). In all other regions, bulk (infinite dilution) diffusion coefficients were used. The resulting piecewise constant profile was smoothed as described (20).

For  $\text{K}^+$  the three diffusion coefficients were determined by reproducing the experimental current in symmetric 250 mM KCl in native RyR (80 pA at +100 mV) and in the mutants E4900Q (10 pA at +20 mV) and D4839N (52 pA at +100 mV). The diffusion  $\text{K}^+$  coefficients (from cytosolic to luminal)

were  $122.1 \times 10^{-11}$ ,  $6.91 \times 10^{-11}$ , and  $40.3 \times 10^{-11} \text{ m}^2/\text{s}$ . For all non- $\text{K}^+$  cations ( $\text{Li}^+$ ,  $\text{Na}^+$ ,  $\text{Rb}^+$ ,  $\text{Cs}^+$ ,  $\text{Mg}^{2+}$ , and  $\text{Ca}^{2+}$ ) only one diffusion coefficient was left undetermined by assuming that the ratio of bulk to cytosolic vestibule diffusion coefficients for  $\text{K}^+$  was the same as for all other cations and by assuming that the ratio of selectivity filter to luminal vestibule diffusion coefficients for  $\text{K}^+$  was the same for all other cations. The one open diffusion coefficient in the selectivity filter was determined for the monovalent cations by reproducing the current at +100 mV in 250 mM symmetric conditions:  $\text{Li}^+$  (21.2 pA),  $\text{Na}^+$  (48.1 pA),  $\text{Rb}^+$  (71.5 pA), and  $\text{Cs}^+$  (51.9 pA). For the divalent cations, the selectivity filter diffusion coefficient was determined by reproducing the current at -100 mV in 250 mM symmetric KCl and 10 mM luminal divalent-chloride:  $\text{Mg}^{2+}$  (-31 pA) and  $\text{Ca}^{2+}$  (-33 pA). The selectivity filter diffusion coefficients were found to be:  $1.29 \times 10^{-11}$  for  $\text{Li}^+$ ,  $3.65 \times 10^{-11}$  for  $\text{Na}^+$ ,  $6.91 \times 10^{-11}$  for  $\text{K}^+$ ,  $5.92 \times 10^{-11}$  for  $\text{Rb}^+$ ,  $4.18 \times 10^{-11}$  for  $\text{Cs}^+$ ,  $0.42 \times 10^{-11}$  for  $\text{Mg}^{2+}$ , and  $0.41 \times 10^{-11} \text{ m}^2/\text{s}$  for  $\text{Ca}^{2+}$ .

While no molecular dynamics simulations to determine diffusion coefficients inside a highly-charged calcium channel have been performed, these values for the selectivity filter diffusion coefficients are consistent with those used in other models of RyR (17–19) and consistent with diffusion coefficients used in models of other highly-charged ion channels (13,24,26,64,65) and of other channels (66–70). Diffusion coefficients in highly-charged pores like RyR have never been simulated, so it is unclear how large they are. It is known, however, that concentrating electrolytes can significantly reduce their diffusion coefficients (71,72).

With some simplifying assumptions, one can also do a back-of-the-envelope calculation to determine the order of magnitude of the selectivity filter diffusion coefficients. Assuming that the one-dimensional Nernst-Planck equation applies and that the baths are identical, one can integrate Eq. 4 to give

$$g_i = \frac{z_i^2 e^2}{kT} \left[ \int (D_i A \rho_i)^{-1} dx \right]^{-1}, \quad (9)$$

where the conductance  $g_i = z_i e J_i / V$ . If the flux is limited in the selectivity filter where the diffusion coefficient and area are constant and if the cation density is also assumed constant, then

$$g_i = \frac{z_i^2 e^2 D_i A \rho_i}{kT L}, \quad (10)$$

where  $L$  is the length of the selectivity filter. If there is only one cation species as the charge carrier, then charge neutrality gives  $\rho_i \approx Q/z_i A L$  where  $Q$  is the number of negative protein charges in the selectivity filter. Then

$$g_i = \frac{z_i e^2 D_i Q}{kT L^2}. \quad (11)$$

(Note that this estimate is independent of how the chemical potential is calculated.) In RyR,  $\text{K}^+$  has a conductance of 800 pS (45). This corresponds to  $D_K = 7.3 \times 10^{-11} \text{ m}^2/\text{s}$  for a 15 Å-long selectivity filter with four negative protein charges—very close to the  $6.91 \times 10^{-11} \text{ m}^2/\text{s}$  used in the model. Similarly, for  $\text{Ca}^{2+}$  with a conductance of 120 pS (Supplementary Material Fig. S9A–C, open triangles),  $D_{Ca} = 0.54 \times 10^{-11} \text{ m}^2/\text{s}$ —which is close to the  $0.41 \times 10^{-11} \text{ m}^2/\text{s}$  used in the model. It is usually estimated that diffusion coefficients in narrow pores are reduced by at most a factor 10 from bulk. In this case, because the ion density  $\rho_i$  is very large (13 M for the Asp-4899 region (20)), if the diffusion coefficient is reduced by only a factor 10 from bulk, then the  $\text{K}^+$  conductance would be ~2200 pS—2.75 times too large.

After determining the three diffusion coefficients for  $\text{K}^+$  and one diffusion coefficient for  $\text{Li}^+$ ,  $\text{Na}^+$ ,  $\text{Rb}^+$ ,  $\text{Cs}^+$ ,  $\text{Mg}^{2+}$ , and  $\text{Ca}^{2+}$  using exactly nine experimental data points out of more than a thousand, the model reproduces all the permeation and selectivity data of RyR2 (the cardiac isoform of RyR) in over 100 different ionic solutions—some yet to be published—without readjusting any parameters. The comparison of the revised model and experimental data for two mole fraction curves and 55 current/voltage curves in pure monovalent-chloride, bi-ionic, and

monovalent/divalent mixtures in native and mutant RyR of Gillespie et al. (20) are shown here and in the main text. Comparisons of model results and previously unpublished experiment data will be published later.

The additional structural and mutation data have substantially improved the results of the model. The new model also reproduces the conductances of mutations not in the previous model without any adjustable parameters; in 250 mM symmetric KCl, the model conductance is 718 pS for D4945N (experimental  $737 \pm 11$  pS (43)) and 792 pS for E4902Q (experimental  $782 \pm 4$  pS (42)).

Details of the modeling not described here are discussed in Gillespie et al. (20).

Supplementary Material Figs. S1–S9 show the results of the model compared to experiments in 66 ionic solutions in both native and three mutants (D4899N, E4900Q, and D4938N). These experimental data have been published previously (20,42,43) and many were compared to the previous model (20). Supplementary Material Figs. S1–S9 compare this same data to the new model because there were important improvements in many cases (see figure captions). While not all comparisons showed improvement, the entire data set is included for completeness.

The Supplementary Material also discusses the model's self-consistency and possible errors.

## SUPPLEMENTARY MATERIAL

To view all of the supplemental files associated with this article, visit [www.biophysj.org](http://www.biophysj.org).

The author is extremely grateful to Prof. Michael Fill and his lab (especially Alma Nani) for performing the experiments on the anomalous mole fraction predictions and for performing them so quickly. Many thanks to Prof. Gerhard Meissner and his lab (especially Le Xu) for wonderful discussions and for providing the experimental data that made this model possible. Also thanks to Montserrat Samsó for very helpful conversations on RyR structure. Useful comments on the manuscript from Wolfgang Nonner, Bob Eisenberg, Dezső Boda, and Michael Fill are also gratefully acknowledged.

The author was supported through National Institutes of Health grant No. 5-R01-GM076013 (Robert Eisenberg, PI).

## REFERENCES

- Hess, P., J. B. Lansman, and R. W. Tsien. 1986. Calcium channel selectivity for divalent and monovalent cations. Voltage and concentration dependence of single channel current in ventricular heart cells. *J. Gen. Physiol.* 88:293–319.
- Almers, W., E. W. McCleskey, and P. T. Palade. 1984. A non-selective cation conductance in frog muscle membrane blocked by micromolar external calcium ions. *J. Physiol. (Lond.)* 353:565–583.
- Almers, W., and E. W. McCleskey. 1984. Non-selective conductance in calcium channels of frog muscle: calcium selectivity in a single-file pore. *J. Physiol. (Lond.)* 353:585–608.
- Smith, J. S., R. Coronado, and G. Meissner. 1985. Sarcoplasmic reticulum contains adenine nucleotide-activated calcium channels. *Nature* 316:446–449.
- Heinemann, S. H., H. Terlau, W. Stuhmer, K. Imoto, and S. Numa. 1992. Calcium channel characteristics conferred on the sodium channel by single mutations. *Nature* 356:441–443.
- Yang, J., P. T. Ellinor, W. A. Sather, J.-F. Zhang, and R. Tsien. 1993. Molecular determinants of  $\text{Ca}^{2+}$  selectivity and ion permeation in L-type  $\text{Ca}^{2+}$  channels. *Nature* 366:158–161.
- Gao, L., D. Balshaw, L. Xu, A. Tripathy, C. Xin, and G. Meissner. 2000. Evidence for a role of the lumenal M3–M4 loop in skeletal muscle  $\text{Ca}^{2+}$  release channel (ryanodine receptor). Activity and conductance. *Biophys. J.* 79:828–840.
- Boda, D., D. D. Busath, D. J. Henderson, and S. Sokolowski. 2000. Monte Carlo simulations of the mechanism of channel selectivity: the competition between volume exclusion and charge neutrality. *J. Phys. Chem. B* 104:8903–8910.
- Boda, D., D. Henderson, and D. D. Busath. 2001. Monte Carlo study of the effect of ion and channel size on the selectivity of a model calcium channel. *J. Phys. Chem. B* 105:11574–11577.
- Boda, D., D. Henderson, and D. D. Busath. 2002. Monte Carlo study of the selectivity of calcium channels: improved geometry. *Mol. Phys.* 100:2361–2368.
- Boda, D., M. Valiskó, B. Eisenberg, W. Nonner, D. J. Henderson, and D. Gillespie. 2006. The effect of protein dielectric coefficient on the ionic selectivity of a calcium channel. *J. Chem. Phys.* 125:034901.
- Boda, D., M. Valiskó, B. Eisenberg, W. Nonner, D. J. Henderson, and D. Gillespie. 2007. Combined effect of pore radius and protein dielectric coefficient on the selectivity of a calcium channel. *Phys. Rev. Lett.* 98:168102.
- Nonner, W., and B. Eisenberg. 1998. Ion permeation and glutamate residues linked by Poisson-Nernst-Planck theory in L-type calcium channels. *Biophys. J.* 75:1287–1305.
- Nonner, W., L. Catacuzzeno, and B. Eisenberg. 2000. Binding and selectivity in L-type calcium channels: a mean spherical approximation. *Biophys. J.* 79:1976–1992.
- Corry, B., T. W. Allen, S. Kuyucak, and S.-H. Chung. 2001. Mechanisms of permeation and selectivity in calcium channels. *Biophys. J.* 80:195–214.
- Corry, B., T. Vora, and S.-H. Chung. 2005. Electrostatic basis of valence selectivity in cationic channels. *Biochim. Biophys. Acta BBA Biomembr.* 1711:72–86.
- Chen, D., L. Xu, A. Tripathy, G. Meissner, and B. Eisenberg. 1997. Permeation through the calcium release channel of cardiac muscle. *Biophys. J.* 73:1337–1354.
- Chen, D. P., L. Xu, A. Tripathy, G. Meissner, and B. Eisenberg. 1999. Selectivity and permeation in calcium release channel of cardiac muscle. Alkali metal ions. *Biophys. J.* 76:1346–1366.
- Chen, D., L. Xu, B. Eisenberg, and G. Meissner. 2003. Calcium ion permeation through the calcium release channel (ryanodine receptor) of cardiac muscle. *J. Phys. Chem. B* 107:9139–9145.
- Gillespie, D., L. Xu, Y. Wang, and G. Meissner. 2005. (De)constructing the ryanodine receptor: modeling ion permeation and selectivity of the calcium release channel. *J. Phys. Chem. B* 109:15598–15610.
- Nonner, W., D. Gillespie, D. J. Henderson, and B. Eisenberg. 2001. Ion accumulation in a biological calcium channel: effects of solvent and confining pressure. *J. Phys. Chem. B* 105:6427–6436.
- Gillespie, D., W. Nonner, and R. S. Eisenberg. 2002. Coupling Poisson-Nernst-Planck and density functional theory to calculate ion flux. *J. Phys. Condens. Matter* 14:12129–12145.
- Corry, B., M. Hoyle, T. W. Allen, M. Walker, S. Kuyucak, and S.-H. Chung. 2002. Reservoir boundaries in Brownian dynamics simulations of ion channels. *Biophys. J.* 82:1975–1984.
- Miedema, H., A. Meter-Arkema, J. Wierenga, J. Tang, B. Eisenberg, W. Nonner, H. Hektor, D. Gillespie, and W. Meijberg. 2004. Permeation properties of an engineered bacterial OmpF porin containing the EEEE-luciferase of  $\text{Ca}^{2+}$  channels. *Biophys. J.* 87:3137–3147.
- Vrouenraets, M., J. Wierenga, W. Meijberg, and H. Miedema. 2006. Chemical modification of the bacterial porin OmpF: gain of selectivity by volume reduction. *Biophys. J.* 90:1202–1211.
- Miedema, H., M. Vrouenraets, J. Wierenga, D. Gillespie, B. Eisenberg, W. Meijberg, and W. Nonner. 2006.  $\text{Ca}^{2+}$  Selectivity of a chemically modified OmpF with reduced pore volume. *Biophys. J.* 91:4392–4400.
- Marconi, U. M. B., and P. Tarazona. 1999. Dynamic density functional theory of fluids. *J. Chem. Phys.* 110:8032–8044.
- Penna, F., and P. Tarazona. 2003. Dynamic density functional theory for steady currents: application to colloidal particles in narrow channels. *J. Chem. Phys.* 119:1766–1776.

29. Archer, A. 2006. Dynamical density functional theory for dense atomic liquids. *J. Phys. Condens. Matter.* 18:5617–5628.
30. Schuss, Z., B. Nadler, and B. Eisenberg. 2001. Derivation of Poisson and Nernst-Planck equations in a bath and channel from a molecular model. *Phys. Rev. E.* 64:036116.
31. Waisman, E., and J. L. Lebowitz. 1970. Exact solution of an integral equation for the structure of a primitive model of an electrolyte. *J. Chem. Phys.* 52:4307–4309.
32. Wu, J. 2006. Density functional theory for chemical engineering: from capillarity to soft materials. *AIChE J.* 52:1169–1193.
33. Rosenfeld, Y. 1993. Free energy model for inhomogeneous fluid mixtures: Yukawa-charged hard spheres, general interactions, and plasmas. *J. Chem. Phys.* 98:8126–8148.
34. Gillespie, D., W. Nonner, and R. S. Eisenberg. 2003. Density functional theory of charged, hard-sphere fluids. *Phys. Rev. E.* 68:031503.
35. Barthel, J. M. G., H. Krienke, and W. Kunz. 1998. *Physical Chemistry of Electrolyte Solutions: Modern Aspects*. Springer, New York.
36. Evans, R. 1992. Density functionals in the theory of nonuniform fluids. In *Fundamentals of Inhomogeneous Fluids*. D. J. Henderson, editor. Marcel Dekker, New York.
37. Berry, S. R., S. A. Rice, and J. Ross. 2000. *Physical Chemistry*. Oxford, New York.
38. Li, Z., and J. Wu. 2004. Density-functional theory for the structures and thermodynamic properties of highly asymmetric electrolyte and neutral component mixtures. *Phys. Rev. E.* 70:031109.
39. Gillespie, D., M. Valiskó, and D. Boda. 2005. Density functional theory of the electrical double layer: the RFD functional. *J. Phys. Condens. Matter.* 17:6609–6626.
40. Valiskó, M., D. Boda, and D. Gillespie. 2007. Selective adsorption of ions with different diameter and valence at highly-charged interfaces. *J. Phys. Chem. C.* 111:15575–15585.
41. Gillespie, D. 1999. *A Singular Perturbation Analysis of the Poisson-Nernst-Planck System: Applications to Ionic Channels*. Rush University, Chicago, IL.
42. Wang, Y., L. Xu, D. A. Pasek, D. Gillespie, and G. Meissner. 2005. Probing the role of negatively charged amino acid residues in ion permeation of skeletal muscle ryanodine receptor. *Biophys. J.* 89:256–265.
43. Xu, L., Y. Wang, D. Gillespie, and G. Meissner. 2006. Two rings of negative charges in the cytosolic vestibule of type-1 ryanodine receptor modulate ion fluxes. *Biophys. J.* 90:443–453.
44. Kettlun, C., A. Gonzalez, E. Ríos, and M. Fill. 2003. Unitary  $\text{Ca}^{2+}$  Current through mammalian cardiac and amphibian skeletal muscle ryanodine receptor channels under near-physiological ionic conditions. *J. Gen. Physiol.* 122:407–417.
45. Lindsay, A. R., S. D. Manning, and A. J. Williams. 1991. Monovalent cation conductance in the ryanodine receptor-channel of sheep cardiac muscle sarcoplasmic reticulum. *J. Physiol. (Lond.)* 439:463–480.
46. Tinker, A., and A. J. Williams. 1992. Divalent cation conduction in the ryanodine receptor channel of sheep cardiac muscle sarcoplasmic reticulum. *J. Gen. Physiol.* 100:479–493.
47. Xu, L., and G. Meissner. 1998. Regulation of cardiac muscle  $\text{Ca}^{2+}$  release channel by sarcoplasmic reticulum lumenal  $\text{Ca}^{2+}$ . *Biophys. J.* 75:2302–2312.
48. Hille, B. 2001. *Ion Channels of Excitable Membranes*. Sinauer Associates, Sunderland, MA.
49. Lundstrom, M. 2000. *Fundamentals of Carrier Transport*. Cambridge University Press, New York.
50. Chen, D. P., R. S. Eisenberg, J. W. Jerome, and C. W. Shu. 1995. Hydrodynamic model of temperature change in open ionic channels. *Biophys. J.* 69:2304–2322.
51. Hänggi, P., P. Talkner, and M. Borokovec. 1990. Reaction-rate theory: fifty years after Kramers. *Rev. Mod. Phys.* 62:251–341.
52. Eisenberg, R. S., M. M. Klosek, and Z. Schuss. 1995. Diffusion as a chemical reaction: stochastic trajectories between fixed concentrations. *J. Chem. Phys.* 102:1767–1780.
53. Eisenberg, R. S. 1999. From structure to function in open ionic channels. *J. Membr. Biol.* 171:1–24.
54. Shannon, R. D., and C. T. Prewitt. 1969. Effective ionic radii in oxides and fluorides. *Acta Crystallogr.* B25:925–946.
55. Boda, D., W. Nonner, M. Valisko, D. Henderson, B. Eisenberg, and D. Gillespie. 2007. Steric selectivity in Na channels arising from protein polarization and mobile side chains. *Biophys. J.* 93:1960–1980.
56. Woelki, S., and H.-H. Kohler. 2000. A modified Poisson-Boltzmann equation. II. Models and solutions. *Chem. Phys.* 261:421–438.
57. Noskov, S. Y., and B. Roux. 2007. Importance of hydration and dynamics on the selectivity of the KcsA and NaK channels. *J. Gen. Physiol.* 129:135–143.
58. Varma, S., and S. Rempe. 2007. Tuning ion coordination architectures to enable selective partitioning. *Biophys. J.* 93:1093–1099.
59. Boda, D., D. Busath, B. Eisenberg, D. J. Henderson, and W. Nonner. 2002. Monte Carlo simulations of ion selectivity in a biological  $\text{Na}^{+}$  channel: charge-space competition. *Phys. Chem. Chem. Phys.* 4:5154–5160.
60. McCleskey, E. W., and W. Almers. 1985. The Ca channel in skeletal muscle is a large pore. *Proc. Natl. Acad. Sci. USA.* 82:7149–7153.
61. Lepsik, M., and M. J. Field. 2007. Binding of calcium and other metal ions to the EF-hand loops of calmodulin studied by quantum chemical calculations and molecular dynamics simulations. *J. Phys. Chem. B.* 111:10012–10022.
62. Ludtke, S. J., I. I. Serysheva, S. L. Hamilton, and W. Chiu. 2005. The pore structure of the closed RyR1 channel. *Structure.* 13:1203–1211.
63. Samsó, M., T. Wagenknecht, and P. D. Allen. 2005. Internal structure and visualization of transmembrane domains of the RyR1 calcium release channel by cryo-EM. *Nat. Struct. Mol. Biol.* 12:539–544.
64. Chen, D., J. Lear, and B. Eisenberg. 1997. Permeation through an open channel: Poisson-Nernst-Planck theory of a synthetic ionic channel. *Biophys. J.* 72:97–116.
65. Rodriguez-Contreras, A., W. Nonner, and E. N. Yamoah. 2002.  $\text{Ca}^{2+}$  transport properties and determinants of anomalous mole fraction effects of single voltage-gated  $\text{Ca}^{2+}$  channels in hair cells from bullfrog sacculus. *J. Physiol.* 538:729–745.
66. Hollerbach, U., D. P. Chen, D. D. Busath, and B. Eisenberg. 2000. Predicting function from structure using the Poisson-Nernst-Planck equations: sodium current in the Gramicidin A channel. *Langmuir.* 16:5509–5514.
67. Cardenas, A. E., R. D. Coalson, and M. G. Kurnikova. 2000. Three-dimensional Poisson-Nernst-Planck theory studies: influence of membrane electrostatics on Gramicidin A channel conductance. *Biophys. J.* 79: 80–93.
68. Furini, S., F. Zerbetto, and S. Cavalcanti. 2006. Application of the Poisson-Nernst-Planck theory with space-dependent diffusion coefficients to KcsA. *Biophys. J.* 91:3162–3169.
69. Mamonov, A. B., M. G. Kurnikova, and R. D. Coalson. 2006. Diffusion constant of  $\text{K}^{+}$  inside Gramicidin A: a comparative study of four computational methods. *Biophys. Chem.* 124:268–278.
70. Bostick, D., and M. L. Berkowitz. 2003. The implementation of slab geometry for membrane-channel molecular dynamics simulations. *Biophys. J.* 85:97–107.
71. Laudernet, Y., T. Cartailier, P. Turq, and M. Ferrario. 2003. A microscopic description of concentrated potassium fluoride aqueous solutions by molecular dynamics simulation. *J. Phys. Chem. B.* 107: 2354–2361.
72. Allen, T. W., S. Kuyucak, and S.-H. Chung. 2000. Molecular dynamics estimates of ion diffusion in model hydrophobic and KcsA potassium channels. *Biophys. Chem.* 86:1–14.